

A 2% Distance to $z = 0.35$ by Reconstructing Baryon Acoustic Oscillations - II: Fitting Techniques

Xiaoying Xu¹, Nikhil Padmanabhan², Daniel J. Eisenstein³, Kushal T. Mehta¹, Antonio J. Cuesta²

¹ *Steward Observatory, University of Arizona, 933 N. Cherry Ave., Tucson, AZ 85721; xxu@as.arizona.edu*

² *Dept. of Physics, Yale University, 260 Whitney Ave., New Haven, CT 06511*

³ *Harvard Smithsonian Center for Astrophysics, Harvard University, 60 Garden St., Cambridge, MA 02138*

20 August 2018

ABSTRACT

We present results from fitting the baryon acoustic oscillation (BAO) signal in the correlation function obtained from the first application of reconstruction to a galaxy redshift survey, namely, the Sloan Digital Sky Survey (SDSS) Data Release 7 (DR7) luminous red galaxy (LRG) catalogue. We also introduce more careful approaches for deriving a suitable covariance matrix and fitting model for galaxy correlation functions. These all aid in obtaining a more accurate measurement of the acoustic scale and its error. We validate our reconstruction, covariance matrix and fitting techniques on 160 mock catalogues derived from the LasDamas simulations in real and redshift space. We then apply these techniques to the DR7 LRG sample and find that the error on the acoustic scale decreases from $\sim 3.5\%$ before reconstruction to $\sim 1.9\%$ after reconstruction. This factor of 1.8 reduction in the error is equivalent to the effect of tripling the survey volume. We also see an increase in our BAO detection confidence from $\sim 3\sigma$ to $\sim 4\sigma$ after reconstruction with our confidence level in measuring the correct acoustic scale increasing from $\sim 3\sigma$ to $\sim 5\sigma$. Using the mean of the acoustic scale probability distributions produced from our fits, we find $D_v/r_s = 8.89 \pm 0.31$ before reconstruction and 8.88 ± 0.17 after reconstruction.

Key words: distance scale – cosmological parameters – large-scale structure of universe – cosmology: theory, observations

1 INTRODUCTION

The interaction between matter and radiation prior to cosmological recombination leaves an imprint on the present day distribution of matter known as the baryon acoustic oscillations (BAO). As matter accreted in overdensities under the influence of gravity, the resulting compression of the primordial plasma caused temperatures and hence radiation pressure to increase. When the radiation pressure became sufficiently high, the photons pushed out from the overdensities in spherical sound waves carrying the baryons along with them. The subsequent competition between gravity and radiation pressure set up a system of standing sound waves within the primordial plasma (Peebles & Yu 1970; Sunyaev & Zeldovich 1970; Bond & Efstathiou 1984; Holtzman 1989; Hu & Sugiyama 1996; Hu & White 1996; Eisenstein & Hu 1998). The frequency of these waves corresponds to a characteristic spatial scale known as the acoustic scale or the sound horizon. This is the distance traveled by the sound wave in the plasma before recombination and is ~ 150 comoving Mpc. After

the photons stream off, the baryons are deposited at these characteristic separations which can still be seen in the galaxy distribution today. Therefore, this acoustic scale can be used as a very accurate standard ruler for measuring cosmological distances at large spatial separations (Eisenstein & Hu 1998; Eisenstein, Hu & Tegmark 1998; Blake & Glazebrook 2003; Eisenstein 2003; Hu & Haiman 2003; Linder 2003; Seo & Eisenstein 2003; Matsubara 2004; Abdalla & Rawlings 2005; Amendola, Quercellini & Giallongo 2005; Angulo et al. 2005; Glazebrook & Blake 2005; Dolney, Jain & Takada 2006). This has been demonstrated using galaxy redshift surveys such as described in Cole et al. (2005); Eisenstein et al. (2005); Hütsi (2006); Tegmark et al. (2006); Padmanabhan et al. (2007); Percival et al. (2007a,b); Sanchez et al. (2009); Kazin et al. (2010); Percival et al. (2010); Beutler et al. (2011); Blake et al. (2011a,b); Ho et al. (2012); Seo et al. (2012). Forecasts have also been made for BAO studies in future galaxy surveys (e.g. Wang et al. 2009; Hu, Knox & Tyson 2009)

and neutral hydrogen surveys (e.g. Mao & Wu 2008; Wyithe, Loeb & Geil 2008).

In practice, the acoustic scale may appear slightly shifted from its predicted linear theory position due to non-linear structure growth (Meiksin, White & Peacock 1999; Seo & Eisenstein 2005; Jeong & Komatsu 2006; Eisenstein, Seo & White 2007; Huff et al. 2007; Guzik, Bernstein & Smith 2007; Ma 2007; Angulo et al. 2008; Crocce & Scoccimarro 2008; Sanchez, Baugh & Angulo 2008; Seo et al. 2008; Smith, Scoccimarro, & Sheth 2008; Padmanabhan & White 2009). Non-linear evolution may also smear the acoustic peak making it more difficult to centroid, thereby resulting in a poorer measurement of the acoustic scale. However, these uncertainties can be largely removed by reconstruction (Eisenstein et al. 2007; Seo et al. 2008; Noh et al. 2009; Padmanabhan, White & Cohn 2009; Seo et al. 2010; Mehta et al. 2011), which is the process by which galaxies are moved back along the first-order displacements that arise due to non-linear growth. In addition to partially undoing non-linear structure growth, our reconstruction technique also includes a prescription to remove the large-scale redshift-space distortion (known as Kaiser squashing; Kaiser 1987) that further distorts the BAO signal along the line-of-sight. This paper along with its companion papers, Padmanabhan et al. (2012, in prep) and Mehta et al. (2012, in prep), presents the first application of reconstruction to a galaxy redshift survey.

Since the goal of all BAO galaxy surveys is to measure the acoustic scale to high precision, we intend for this paper to present a viable procedure for attaining this goal. We include a discussion of the necessary statistical tools, such as a new method for deriving a reliable, smooth covariance matrix, and a robust fitting framework for measuring the acoustic scale. We use our mock catalogues to demonstrate that making slight adjustments to our fiducial model parameters such as Σ_{nl} (used to model the degradation of the BAO signal due to non-linear structure growth), the fitting range, the number of marginalization terms and the input cosmology, do not alter the measured acoustic scale. This indicates the robustness of our techniques.

Using these tools and the DR7 LRG sample, we measure the acoustic scale to 3.5% before reconstruction and 1.9% after reconstruction. Our post-reconstruction result is the highest precision measurement of the acoustic scale at $z = 0.35$ obtained through galaxy surveys to date. Without reconstruction, we would need to increase the survey volume by nearly a factor of 3 to achieve this same factor of 1.8 reduction in the error. We also find that both measures of BAO significance we consider improve by at least 1σ after reconstruction.

In §2 we discuss the mock catalogues we use for our analyses and our reconstruction parameters. In §3 we describe some of the covariance and fitting techniques used in previous studies followed by an outline of the covariance matrix and fitting models we employ for this study. §4 describes the fitting results on our redshift-space mocks. The analogous discussion for real space is found in §5. We apply our techniques to the DR7 LRG sample in §6 and conclude in §7. For more details of the reconstruction method and the SDSS data set, we refer the interested reader to the companion paper Padmanabhan et al. (2012, in prep) (Pa-

per I). The DR7 cosmology results can be found in the other companion paper Mehta et al. (2012, in prep) (Paper III).

2 MOCK CATALOGUES AND RECONSTRUCTION

A variety of statistics such as the correlation function, the power spectrum, and more recently $\omega_\ell(r_s)$ (Xu et al. 2010) are available for measuring clustering and the BAO scale. As mentioned in §1, the measurement of this scale is affected by non-linear structure growth. Hence, in order to obtain an accurate measurement of the acoustic scale through fitting the observational data, we must first employ an algorithm known as reconstruction to partially undo the effects of this non-linear evolution. We also need to develop a technique that returns reliable error estimates for our chosen clustering statistic (i.e. the covariances between different scales) and a method to marginalize out the broadband (non-BAO) information from the statistic.

To this end, we compute correlation functions in both real and redshift space with and without reconstruction from SDSS DR7 LRG mock catalogues created using the LasDamas simulations (McBride et al. 2012, in prep). The simulation cosmology is $\Omega_m = 0.25$, $\Omega_b = 0.04$, $h = 0.7$, $n_s = 1$ and $\sigma_{8,\text{matter}} = 0.8$ at $z = 0$. There are a total of 160 mock catalogues corresponding to our area of interest, the DR7 Northern galactic cap, which has a sky coverage of 7189 deg^2 . The redshift range covered by the mocks is $0.16 < z < 0.44$ (note that this is slightly different to the redshift range of the DR7 data, $0.16 < z < 0.47$).

The process of reconstruction is conceptually equivalent to running gravity backwards (Eisenstein et al. 2007). This procedure helps remove some of the smearing and shifting of the acoustic peak caused by non-linear structure growth. We also include a prescription for removing the redshift-space distortion caused by Kaiser squashing which can further broaden the acoustic peak. Many past studies have tested the basic reconstruction algorithm using simulations (Noh et al. 2009; Seo et al. 2010; Mehta et al. 2011), however, this study marks its first application to a real galaxy redshift survey. The reconstruction algorithm can be simply described as follows. We estimate the matter density field from the observed galaxies using a simple bias scaling from the measured galaxy density field. We then solve the linear continuity equation $\nabla \cdot \vec{q} = -\delta$ where \vec{q} is the displacement field and δ is the density field. This gives us the first order displacements that arise from non-linear structure growth. Finally, we shift the galaxies back along these displacement vectors. For our reconstruction, we apply a Gaussian smoothing to the matter density field using a smoothing scale of $15h^{-1} \text{ Mpc}$ to reduce sensitivity to small scale clustering which is poorly constrained in large galaxy surveys.

For details of the computation and reconstruction, please see Paper I. All correlation functions were computed in $3h^{-1} \text{ Mpc}$ bins from $2.5 - 197.5h^{-1} \text{ Mpc}$.

3 COVARIANCE MATRIX AND FITTING TECHNIQUES

3.1 Overview of Past Approaches

In past studies involving observational data, the most common method for deriving the covariance matrix was to construct it from mock catalogues generated from either simulations (Hamilton, Rimes & Scoccimarro 2006; Takahashi et al. 2009) or perturbation theory approaches (Scoccimarro & Sheth 2002). Perturbative methods are less accurate than we would like and as we will show, the covariance matrices calculated from mocks can still be noisy, even if the number of mocks used is large. One can also assume the smooth Gaussian covariance matrix from linear theory, however this neglects the non-linear contribution to the noise. Hence, it is necessary to devise a scheme for approximating the mock covariances with a smooth function or find alternate methods to regularize the matrix. In this paper, we present a robust approximation scheme, which we will show produces a faithful representation of the expected covariances.

The acoustic scale can be measured from galaxy clustering statistics by fitting the data with a template based on linear theory. The location of the acoustic peak in this template must depend on a parameter that specifies the magnitude of the acoustic scale relative to the fiducial value. Typically in Fourier space, this requires a fitting model of the form

$$P(k) = B(k)P_m(k/\alpha) + A(k). \quad (1)$$

Here, $P_m(k)$ is the template power spectrum based on linear theory and α is the scale dilation parameter that is used to adjust the location of the acoustic peak. $A(k)$ and $B(k)$ are functions involving nuisance parameters that can be used to marginalize out the broadband shape of the power spectrum (i.e. scale-dependent bias and redshift-space distortions). The broadband shape does not contain BAO information but may bias the measurement of the BAO scale if not accounted for properly. These terms can also help mitigate the effects of using the wrong model cosmology. Analogously, in configuration space we have

$$\xi(r) = B(r)\xi_m(\alpha r) + A(r). \quad (2)$$

In order to obtain an accurate measure of the acoustic scale, we require this fitting model to be robust. This simply means that if we slightly change the parameters that go into the model, the measured value of α should always be consistent. For a fitting form where this is true, even if we use model parameters that are not optimal, we will still measure the correct acoustic scale. This is necessary since we use this fitting form to derive the acoustic scale in the SDSS DR7 data and in practice we are not certain of the exact model parameters to use.

In Fourier space, Padé approximants and basis functions based on cubic splines work well for both $A(k)$ and $B(k)$, while high order polynomials may also be used for $A(k)$. This has been demonstrated for simulated data (e.g. Seo et al. (2008); Padmanabhan & White (2009); Seo et al. (2010); Mehta et al. (2011)) as well as SDSS-II observational data (e.g. Tegmark et al. (2006); Percival et al. (2007b, 2010)). However, high order polynomials and cubic spline forms do

not transform particularly nicely to configuration space due to poor numerical convergence of the integration.

In configuration space, there have been attempts to model the scale-dependent bias associated with the $B(r)$ term such as in (Blake et al. 2011a). As for $A(r)$, an array of forms have been used. In theoretical works (Crocce & Scoccimarro 2008; Sanchez, Baugh & Angulo 2008) and the DR6 motivated observational work (Sanchez et al. 2009), $A(r)$ was motivated by perturbation theory and contained derivatives and integrations of the linear theory correlation function. Other works based in simulations (e.g. Cabré & Gaztañaga (2011)) and SDSS observations (e.g. Eisenstein et al. (2005); Kazin et al. (2010)) did not use an $A(r)$ term at all. However, as we will show in this work, having a non-zero $A(r)$ term aids greatly in removing unwanted broadband information and ameliorating errors in the assumed model cosmology. This is especially true if one is to take $B(r) = B$ and delegate the marginalization of scale-dependent bias to the $A(r)$ term, as is done in most correlation function analyses. We note here though, that the form for $A(r)$ does not need to be complicated as we show in §3.3.

3.2 Covariance Matrices

We perform the analyses in this paper using the correlation function statistic and hence, we require an estimate of the correlation function covariances. As mentioned previously, the most obvious choice is to use the covariance matrix calculated directly from the mock catalogues. The value of the i th row and j th column of such a covariance matrix is

$$C_{ij} = \frac{1}{N-1} \sum_{n=1}^N [\xi_n(r_i) - \bar{\xi}(r_i)][\xi_n(r_j) - \bar{\xi}(r_j)], \quad (3)$$

where N is the total number of mocks, $\xi_n(r)$ is the correlation function calculated from the n th mock and $\bar{\xi}(r)$ is the average of the mock correlation functions. However, we find that the covariances calculated from 160 mocks are still noisy (see Figure 1). To obtain a smooth approximation to the mock covariances, we introduce a new technique which involves fitting a modified form of the Gaussian covariance matrix to the data using a maximum likelihood approach.

The analytic Gaussian covariance matrix can be calculated as

$$C_{ij} = \frac{2}{V} \int \frac{k^2 dk}{2\pi^2} j_0(kr_i) j_0(kr_j) [P_c(k) + \aleph]^2 \quad (4)$$

where V is the volume of each mock, \aleph is the shot-noise and

$$j_0(kr) = \frac{\sin(kr)}{kr} \quad (5)$$

is the 0th order spherical Bessel function. \aleph has 2 basic components, linear shot-noise and non-linear shot-noise. In the standard Gaussian covariance matrix, the linear shot-noise is assumed to be Poisson, which implies $\aleph_{lin} = \bar{n}^{-1}$. Realistically however, surveys span a range of redshifts, so \bar{n} is dependent on z . In addition, we must also consider the non-linear shot-noise which arises due to non-linear structure growth at small scales. This is typically not included in the calculation of the standard Gaussian covariance matrix. We will address these issues in more detail shortly.

Due to the binning of data in our correlation function

calculations, we must also adjust our Gaussian covariance matrix calculation to reflect this. Theoretically, the value of the binned correlation function at the bin center r_i is

$$\xi(\bar{r}_i) = \frac{\int_{\Omega} \int_{r_{i1}}^{r_{i2}} d^3r \xi(r)}{\int_{\Omega} \int_{r_{i1}}^{r_{i2}} d^3r} \quad (6)$$

$$= \frac{3}{r_{i2}^3 - r_{i1}^3} \int_{\Omega} \int_{r_{i1}}^{r_{i2}} r^2 dr \frac{d\Omega}{4\pi} \int \frac{k^2 dk}{2\pi^2} P(k) j_0(kr) \quad (7)$$

where the bin limits are (r_{i1}, r_{i2}) and $\xi(r)$ is the true unbinned correlation function. Analogously, we may write the expression for the binned covariance matrix as

$$C_{ij} = \frac{2}{V} \frac{3}{r_{i2}^3 - r_{i1}^3} \frac{3}{r_{j2}^3 - r_{j1}^3} \cdot \int_{\Omega} \int_{r_{i1}}^{r_{i2}} r^2 dr \frac{d\Omega}{4\pi} \int_{\Omega'} \int_{r_{j1}}^{r_{j2}} r'^2 dr' \frac{d\Omega'}{4\pi} \cdot \int \frac{k^2 dk}{2\pi^2} j_0(kr_i) j_0(kr_j) [P_c(k) + \aleph]^2. \quad (8)$$

This can be shown to give

$$C_{ij} = \frac{2}{V} \int \frac{k^2 dk}{2\pi^2} \Delta j_1(kr_i) \Delta j_1(kr_j) [P_c(k) + \aleph]^2 \quad (9)$$

where

$$\Delta j_1(kr) = \frac{3}{r_2^3 - r_1^3} \frac{[r_2^2 j_1(kr_2) - r_1^2 j_1(kr_1)]}{k}, \quad (10)$$

$$j_1(kr) = \frac{\sin(kr)}{(kr)^2} - \frac{\cos(kr)}{kr} \quad (11)$$

is the 1st order spherical Bessel function. Here, we have intentionally written Equation (9) to resemble Equation (4).

The input power spectrum $P_c(k)$ determines the sample variance of the signal. In redshift space before reconstruction, we take $P_c(k)$ to have the form,

$$P_c(k) = b_0^2 \int_{-1}^1 (1 + \beta\mu^2)^2 F(\mu, k) P_t(k) d\mu \quad (12)$$

where $(1 + \beta\mu^2)^2$ is the standard Kaiser squashing term (Kaiser 1987) with $\beta = f/b_0$, $f \sim \Omega_m^{0.6}$ and b_0 equal to the large-scale bias. $F(\mu, k)$ is a streaming model term used to account for the Finger of God (FoG) effect. We take this term to be exponential in configuration space and hence

$$F(\mu, k) = \frac{1}{(1 + k^2\mu^2\sigma_s^2)^2} \quad (13)$$

in Fourier space, where σ_s is the dispersion within a cluster and is typically around $3 - 4h^{-1}$ Mpc. A Gaussian form for $F(\mu, k)$ can also be used; however, we find little difference between the results. Kaiser squashing and FoG are known as redshift-space distortions and arise from observational biases in measured redshifts due to motions of galaxies along the line-of-sight direction.

We determine b_0^2 by matching the configuration space transform of $P_c(k)$ to the average of the mock correlation functions at $r = 50h^{-1}$ Mpc. This ensures that the amplitude of $P_c(k)$ matches the average clustering amplitude in the mocks.

Our template power spectrum, $P_t(k)$, takes on the form

$$P_t(k) = [P_{\text{lin}}(k) - P_{\text{smooth}}(k)] e^{-k^2 \Sigma_{\text{nl}}^2 / 2} + P_{\text{smooth}}(k), \quad (14)$$

where $P_{\text{lin}}(k)$ is the linear power spectrum at $z = 0$.

$P_{\text{smooth}}(k)$ is the dewiggled power spectrum described in Eisenstein & Hu (1998) and Σ_{nl} is a smoothing parameter that is used to model the degradation in the acoustic peak due to non-linear evolution (Crocco & Scoccimarro 2006; Eisenstein, Seo & White 2007; Crocco & Scoccimarro 2008; Matsubara 2008; Seo et al. 2008). Before reconstruction, the overall shape of the acoustic peak in the template matches the data best when $\Sigma_{\text{nl}} \sim 8h^{-1}$ Mpc; hence we fix $\Sigma_{\text{nl}} = 8h^{-1}$ Mpc. We will show that varying this value has little affect on the resulting covariance matrix later in this section.

In order to address the z dependence of \bar{n} , we use the fact that Equation (4) is really just the transform of the variance in Fourier space, $[P_c(k) + \aleph]^2 / V$, to the expected covariance in configuration space. One can then imagine building up the inverse of this variance, $I^2(k)$, as an integral over volume,

$$I^2(k) = \int \frac{dV}{[P_c(k) + \aleph]^2} = \frac{c\Omega}{H_0} \int_{z_l}^{z_u} \left[P_c(k) + \frac{1}{\bar{n}(z)} \right]^{-2} \cdot \frac{r^2(z)}{\sqrt{\Omega_m(1+z)^3 + \Omega_\Lambda}} dz, \quad (15)$$

where we use

$$dV = \frac{c}{H_0} \frac{r^2(z)}{\sqrt{\Omega_m(1+z)^3 + \Omega_\Lambda}} dz d\Omega \quad (16)$$

for a flat universe and assume $\bar{n}(z)$ has no angular dependence. z_u and z_l are the upper and lower redshift limits of the survey respectively. Now we can redefine the binned Gaussian covariance matrix, Equation (9), as

$$C_{ij} = 2 \int \frac{k^2 dk}{2\pi^2} \Delta j_1(kr_i) \Delta j_1(kr_j) \mathfrak{P}^2(k) \quad (17)$$

where $\mathfrak{P}^2(k) = [I^2(k)]^{-1}$. We calculate a model for $\bar{n}(z)$ that suits the DR7 data from the LasDamas random catalogue and scale this to other cosmologies when necessary using the appropriate volume ratios.

Since our binned Gaussian covariance matrix does not include non-linear shot-noise, it underpredicts the mock covariance matrix. However, one can imagine applying some modifications to the Gaussian covariance matrix so that its shape better emulates that of the mock covariance matrix. We assume a modification to the Gaussian covariance matrix of

$$C_{ij}^m = 2 \int \frac{k^2 dk}{2\pi^2} \Delta j_1(kr_i) \Delta j_1(kr_j) \mathfrak{P}^2(k; c_0, c_1, c_2) + c_3 \quad (18)$$

where $\mathfrak{P}^2(k; c_0, c_1, c_2)$ corresponds to an $I^2(k)$, Equation (15), in which we make the substitution

$$P_c(k) + \frac{1}{\bar{n}(z)} \rightarrow c_0 P_c(k) + \frac{c_1}{\bar{n}(z)} \int_{-1}^1 (1 + \beta\mu^2)^2 F(\mu, k) d\mu + \frac{c_2}{\bar{n}(z)} = \left[c_0 b_0^2 P_t(k) + \frac{c_1}{\bar{n}(z)} \right] \cdot \int_{-1}^1 (1 + \beta\mu^2)^2 F(\mu, k) d\mu + \frac{c_2}{\bar{n}(z)}. \quad (19)$$

$$\cdot \int_{-1}^1 (1 + \beta\mu^2)^2 F(\mu, k) d\mu + \frac{c_2}{\bar{n}(z)}. \quad (20)$$

The c_0 term accounts for any remaining large-scale bias discrepancies between $P_c(k)$ and the mock data. The c_1 term is used to represent any effects streaming or Kaiser squashing may have on shot-noise. This is associated with non-linear shot-noise. The c_2 term corresponds to the standard Poisson shot-noise from linear theory. The c_0 , c_1 and c_2 are parameters we use to scale the amplitudes of the various components that go into the Gaussian covariance matrix in order to modify its shape and c_3 can be associated with the integral constraint which manifests itself as an additive offset in the correlation function.

The likelihood of any such $C^m(c_0, c_1, c_2, c_3)$ given a set of mock catalogues is

$$\mathcal{L} = \prod_{i=0}^N \mathcal{L}_i \quad (21)$$

$$= \prod_{i=0}^N (2\pi)^{-q/2} (\det C^m)^{-1/2} e^{-\chi_i^2/2} \quad (22)$$

where N is the total number of mocks and q is the number of points to fit. $\chi_i^2 = \vec{x}_i (C^m)^{-1} \vec{x}_i^T$ where $\vec{x}_i = \xi_i(r) - \bar{\xi}(r)$ is a vector of dimension q . $\xi_i(r)$ is the correlation function calculated from the i th mock and $\bar{\xi}(r)$ is the average of the mock correlation functions. Equation (22) can be re-written as

$$L = -2 \log \mathcal{L} = Nq \log(2\pi) + N \log(\det C) + \sum_{i=0}^N \chi_i^2. \quad (23)$$

We would like to find C^m corresponding to the maximum of the likelihood function. This is equivalent to finding the C^m that corresponds to the minimum of L .

Using a downhill simplex minimization scheme and fixing $\sigma_s = 4h^{-1}$ Mpc, we arrive at $c_0 = 0.89$, $c_1 = 0.46$, $c_2 = 1.34$ and $c_3 = 2.32 \times 10^{-7}$ for redshift space before reconstruction. Here, we have fixed the value of σ_s to reduce computation time, however, it is possible to include it as a parameter in the maximum likelihood fit. Allowing σ_s to vary gives $\sigma_s = 3.9h^{-1}$ Mpc with most modification parameters changing by less than 1%. Only c_1 changes by $\sim 3\%$ due to its partial degeneracy with σ_s (when σ_s is increased, a larger damping effect is placed on the power spectrum term which can be compensated for by making c_1 larger). The fact that the likelihood of the fixed σ_s case is 0.99 of the unfixed case also suggests that fixing σ_s is reasonable.

We also investigate the outcome of fixing $c_0 = 1$, i.e. assuming that the sample variance given by our model power spectrum suits the data perfectly. This does not change the log likelihood significantly and we find that the acoustic scales and errors measured from the mocks as well as the DR7 data are consistent with the case where c_0 is allowed to vary. In addition, we find that changing the value of Σ_{n1} that goes into $P_t(k)$ makes very little difference to the resulting covariance matrix. Using $\Sigma_{n1} = 9h^{-1}$ Mpc instead of $\Sigma_{n1} = 8h^{-1}$ Mpc only changes all the modification parameters and the maximum likelihood by $< 1\%$.

The black dots in the top panel of Figure 1 show the diagonal (i.e. the $j = i$ elements) of the mock covariance matrix in redshift space before reconstruction and the black crosses show the corresponding diagonal of the modified Gaussian covariance matrix. Likewise, the 6th off-diagonal (i.e. the $j = i + 6$ elements) is overplotted in red. The noise

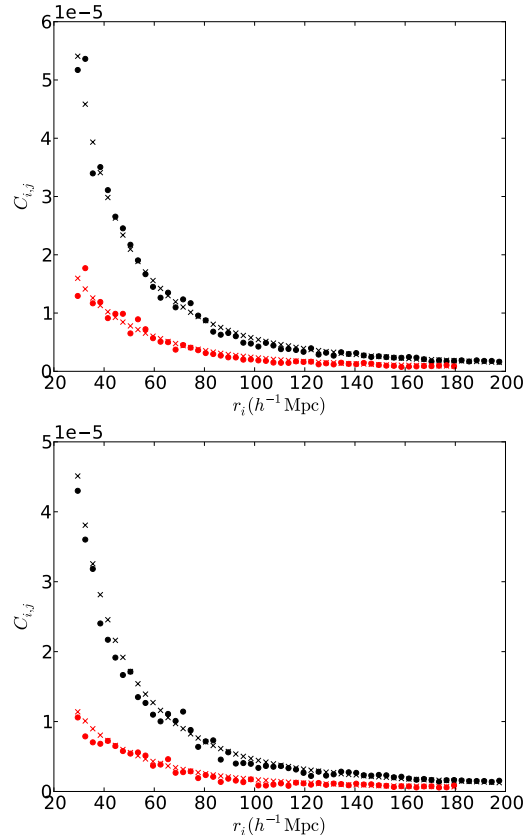


Figure 1. The diagonal (black) and 6th off-diagonal (red) of the mock (circles) and modified Gaussian (crosses) covariance matrices in redshift space before reconstruction (top) and after reconstruction (bottom). The mock covariance matrix shows clear signs of noise. The modified Gaussian covariance matrices take on the form given in Equations (18 & 19) with $\sigma_s = 4h^{-1}$ Mpc. Before reconstruction, $c_0 = 0.89$, $c_1 = 0.46$, $c_2 = 1.34$, $c_3 = 2.32 \times 10^{-7}$ and after reconstruction $c_0 = 0.89$, $c_1 = 0.30$, $c_2 = 1.45$, $c_3 = 1.87 \times 10^{-7}$. One can see that the modified Gaussian covariance matrices are good smoothed approximations to the mock covariance values.

in the mock covariance matrix is obvious. It is evident from the plot that the modified Gaussian covariance matrix is a good smooth approximation to the mock covariance values. Hence, we use the modified Gaussian covariance matrix derived from this maximum likelihood technique with fixed $\sigma_s = 4h^{-1}$ Mpc as our estimate of the expected errors on the mock correlation functions. The fitting technique described in §3.3 utilizes this covariance matrix.

In redshift space after reconstruction, we take the input power spectrum $P_c(k)$ to be

$$P_c(k) = b_0^2 \int_{-1}^1 F(\mu, k) P_t(k) d\mu \quad (24)$$

which is just Equation (12) without the Kaiser term since our reconstruction algorithm is designed to undo Kaiser squashing. We assume $\Sigma_{n1} = 4h^{-1}$ Mpc and retain $\sigma_s = 4h^{-1}$ Mpc since we did not apply any FoG compression. Fitting for the parameters of the modified Gaussian covariance matrix using the maximum likelihood prescription, we find $c_0 = 0.89$, $c_1 = 0.30$, $c_2 = 1.45$, $c_3 = 1.87 \times 10^{-7}$. The diag-

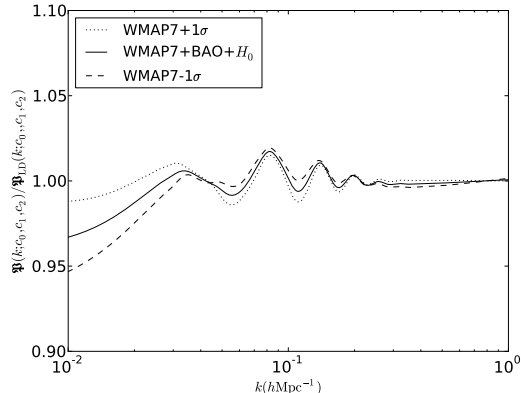


Figure 2. The ratio of $\mathfrak{P}(k; c_0, c_1, c_2)$ terms (see Equation (18) and surrounding text) found in the definition of the modified Gaussian covariance matrix (MGCM). These MGCMs were all fit to the covariances calculated from the LasDamas mocks in redshift space after reconstruction. The numerator corresponds to MGCMs constructed using 3 non-LasDamas cosmologies. The denominator corresponds to the MGCM in the LasDamas cosmology. The 3 non-LasDamas cosmologies are WMAP7+BAO+ H_0 (solid line) and the 1σ limits of this cosmology (+ 1σ is shown as the dotted line and -1σ is shown as the dashed line). It is seen that the 3 lines are all ~ 1 to within $\sim 5\%$. This indicates that if we input a power spectrum with cosmology different to LasDamas, our modification parameters can balance this input and the noise terms to recover a covariance matrix that matches the expected LasDamas covariances fairly well.

onals and 6th off-diagonals of the post-reconstruction mock and modified Gaussian covariance matrices are plotted in the bottom panel of Figure 1. One can see that, as in the pre-reconstruction case, our modified Gaussian approximation fits the mock covariances well.

In the post-reconstruction case, we also test that by using a different cosmology from LasDamas to derive $P_t(k)$, it is still possible to obtain a modified Gaussian covariance matrix that suits the mock data using our maximum likelihood method. In Figure 2, we show $\mathfrak{P}(k; c_0, c_1, c_2)$ for the WMAP7+BAO+ H_0 cosmology (Komatsu et al. 2010) divided by the corresponding LasDamas values (solid line). For reference, the WMAP7 cosmological parameters of relevance are $H_0 = 70.2 \pm 1.4$, $100\Omega_b h^2 = 2.255 \pm 0.054$, $\Omega_c h^2 = 0.1126 \pm 0.0036$, $n_s = 0.968 \pm 0.012$ and $\sigma_8 = 0.816 \pm 0.024$. The dotted (dashed) lines are for cosmologies derived by adding (subtracting) the 1σ errors from the WMAP7 values quoted above. One can see that the 3 lines are all ~ 1 to within $\sim 5\%$ near the acoustic scale indicating that the modification parameters are capable of adjusting the power spectrum and the noise terms in the Gaussian covariance matrix to match the LasDamas covariances. In §4.2, we show that using these different covariance matrices yield consistent acoustic scale measurements and errors to those obtained using the correct LasDamas cosmology.

3.3 Fitting Forms

We fit the mock redshift-space correlation functions $\xi_s(r)$ over the range $30 < r < 200h^{-1}$ Mpc using the fiducial form

(justification to follow)

$$\xi^{fit}(r) = B^2 \xi_m(\alpha r) + A(r) \quad (25)$$

where

$$A(r) = \frac{a_1}{r^2} + \frac{a_2}{r} + a_3. \quad (26)$$

The parameters of the fit are B^2 , α , a_1 , a_2 and a_3 . The latter are linear nuisance parameters.

The scale dilation parameter α represents how much the acoustic peak in the data is shifted relative to that in the model. Therefore, it is our measurement of the acoustic scale and the parameter we are most interested in extracting robustly from our fits. An $\alpha > 1$ indicates a shift towards smaller scales and an $\alpha < 1$ indicates a shift towards larger scales.

The template correlation function, $\xi_m(r)$, takes on the form

$$\xi_m(r) = \int \frac{k^2 dk}{2\pi^2} P_m(k) j_0(kr) e^{-k^2 a^2}, \quad (27)$$

where $P_m(k) = b^2 P_t(k)$ and $P_t(k)$ is defined as in Equation (14). We perform the transformation from Fourier space to configuration space using an additional Gaussian term to provide high- k damping for the oscillatory transform kernel $j_0(kr)$. This is conducive to better numerical convergence in the integration. We pick $a = 1h^{-1}$ Mpc, a scale small enough such that the effects of the damping will not be significant within our fitting range.

The b^2 term is a constant normalization factor that we obtain by taking the ratio of the mock correlation function being fit and the configuration space transform of $P_t(k)$ at $r = 50h^{-1}$ Mpc. This ensures that the fitting normalization B^2 is of order unity. The normalization must be positive, so we perform our fits with the non-linear parameter $\log(B^2)$. Note that B^2 can vary substantially as long as the $A(r)$ function can compensate. This creates large variation in the amplitude of the acoustic peak which is not physically motivated. We find that the scatter in B^2 can be large with values being as high as ~ 2.1 and as low as ~ 0.3 , especially in the mocks where the acoustic signal does not appear to be as strong. This is summarized in Figure 3 where we have plotted B^2 versus best-fit α obtained through fitting the 160 mock correlation functions in redshift space. For a careful description of the information plotted, please see the figure caption. To disfavour extreme values of B^2 , we place a weak Gaussian prior on $\log(B^2)$ with a mean of 0 and standard deviation of 0.4. For simplicity, we also apply this prior to redshift space with reconstruction and real space with and without reconstruction.

We pick the form for $A(r)$ in Equation (26) due to its simplicity in Fourier space. Since the transform of r^n is proportional to k^{-3-n} , in Fourier space $A(r)$ takes on the form

$$A'(k) = \frac{a'_1}{k} + \frac{a'_2}{k^2} + \frac{a'_3}{k^3}. \quad (28)$$

In addition to the fiducial $A(r)$ form in Equation (26), we will also be analyzing various other forms of $A(r)$ throughout this paper. We will refer to $A(r) = A'(k) = 0$ as *poly0*, $A(r) = a_1/r^2$ (first order inverse polynomial in k) as *poly1*, $A(r) = a_1/r^2 + a_2/r$ (second order inverse polynomial in k) as *poly2* and $A(r) = a_1/r^2 + a_2/r + a_3 + a_4 r$ (fourth order

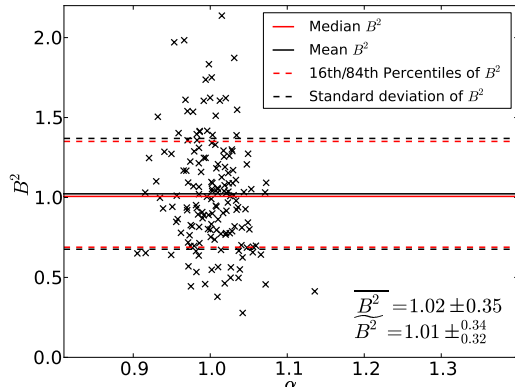


Figure 3. The values of B^2 versus α fit from the mocks in redshift space before reconstruction. To ensure that B^2 is non-negative, these values were obtained through fitting the 160 mock redshift-space correlation functions using the non-linear parameter $\log(B^2)$ instead of B^2 . The solid red line indicates the median B^2 value and the solid black line indicates the mean. The dashed red lines indicate the 16th and 84th percentiles of B^2 (quoted with the median $\overline{B^2}$). The dashed black lines correspond to the 1σ deviations from the mean (quoted with the mean $\overline{B^2}$). One can see that B^2 can reach values as high as ~ 2.1 and as low as ~ 0.3 . This substantial variation is possible because the $A(r)$ term can compensate, and is therefore not physically motivated. Hence to disfavour these extreme values, we place a weak Gaussian prior on $\log(B^2)$ that has mean equal to 0 and standard deviation equal to 0.4.

Table 1. Fit results to average mock correlation functions

	α	Σ_{nl} (h^{-1} Mpc)
Redshift space w/o reconstruction	1.003	8.1
Real space w/o reconstruction	1.002	6.6
Redshift space w/ reconstruction	1.003	4.4
Real space w/ reconstruction	0.999	3.0

inverse polynomial in k) as *poly4*. Note that the fiducial form corresponds to *poly3*.

We find that going up to the constant term in $A(r)$ as in the fiducial form gives a good fit to the average of the mock correlation functions. This is shown in Figure 4 where in the left panel we have plotted the fits to the average mock, redshift-space correlation function (black crosses) using Equation (25) and various forms for $A(r)$. The *poly0*, *poly2*, fiducial form and *poly4* cases are shown as the dotted green, dash-dotted blue, solid black and the dashed red lines respectively. The corresponding residuals are shown in the right panel.

We have also allowed Σ_{nl} to vary in these fits and find that for the fiducial form, $\Sigma_{nl} = 8.1h^{-1}$ Mpc. This is close to the value of $8h^{-1}$ Mpc we assumed in the estimation of the covariance matrix. The results from fits to the mean mock correlation functions using the fiducial form are summarized in Table 1.

The χ^2 per degree-of-freedom (dof) goes down from 2.7 for *poly0* to 1.4 for the fiducial form. The decrease from the fiducial form to *poly4* is much smaller (only ~ 0.2) as

evidenced by the similarity in shape between the solid curve and the dashed curve. Although the value of χ^2 per dof is still large for the fiducial form, we note that the error bars expected when fitting each individual mock will be much larger and thus result in reasonable values of χ^2 as will be shown in §4.1. In principle we could further lower χ^2 by taking $A(r)$ out to higher orders of r , however we then run the risk of having the nuisance parameters fit the noise in the data.

Recall that our ultimate goal is to measure the acoustic scale, α , from the data. This can be done by finding the value of α that gives rise to the best-fit model to the data. Our models are non-linear in α and the normalization factor $\log(B^2)$, so we can nest a linear least-squares fitter inside a non-linear fitting routine, which in our case is a downhill simplex. The former calculates a_1 , a_2 and a_3 for each value of α and B^2 the latter steps to. Then, to find the best-fit α , we use the non-linear fitter to minimize the χ^2 goodness-of-fit indicator

$$\chi^2(\alpha, B^2) = [\vec{d} - \vec{m}(\alpha, B^2)]^T C^{-1} [\vec{d} - \vec{m}(\alpha, B^2)] \quad (29)$$

where \vec{d} is the correlation function measured from the mocks and $\vec{m}(\alpha, B^2)$ is the best-fit model at each α and B^2 . C^{-1} is the inverse of the covariance matrix. Recall that we use the modified Gaussian covariance matrix (MGCM) described in Equation (18) of §3.2 here.

Based on our fiducial form defined in Equations (25 & 26), we define a fiducial model for redshift space over a fitting range of $30 < r < 200h^{-1}$ Mpc. $\xi_m(k)$ is derived from the LasDamas cosmology using $\Sigma_{nl} = 8h^{-1}$ Mpc. We denote the fiducial model with subscript [*f*] throughout this paper unless otherwise stated. We perform the above prescribed fitting algorithm on all 160 of our mock catalogues using the fiducial model to obtain a best-fit value of α for each.

For redshift space with reconstruction, we use the same fiducial fitting form defined by Equations (25 & 26). The mean of the mock redshift-space correlation functions before (black) and after (red) reconstruction are shown in Figure 5. The data are represented by crosses and the fits to the data using the fiducial fitting form are shown as solid lines. The results from these fits are also summarized in Table 1.

Since before reconstruction, α is already very close to 1, we would not expect reconstruction to have a large affect on the measured acoustic scale, which is exactly what we see. However, we find that after reconstruction, $\Sigma_{nl} = 4.4h^{-1}$ Mpc, which is a factor of 1.8 reduction from its pre-reconstruction value of $\Sigma_{nl} = 8.1h^{-1}$ Mpc. This decrease in Σ_{nl} indicates that reconstruction was successful at reducing the smearing (large Σ_{nl}) of the acoustic peak caused by non-linear structure growth. Visually, this can be seen as the sharpening of the acoustic feature in the average of the mocks after reconstruction. A sharpened peak is easier to centroid and should result in a more accurate measurement of the acoustic scale.

We define the fiducial model in redshift space after reconstruction to be identical to the pre-reconstruction model except with $\Sigma_{nl} = 4h^{-1}$ Mpc. This is the same value as that used to derive the MGCM for post-reconstruction redshift space. This is not a bad approximation as we have just shown the fit to the average of the mock correlation functions has $\Sigma_{nl} = 4.4h^{-1}$ Mpc.

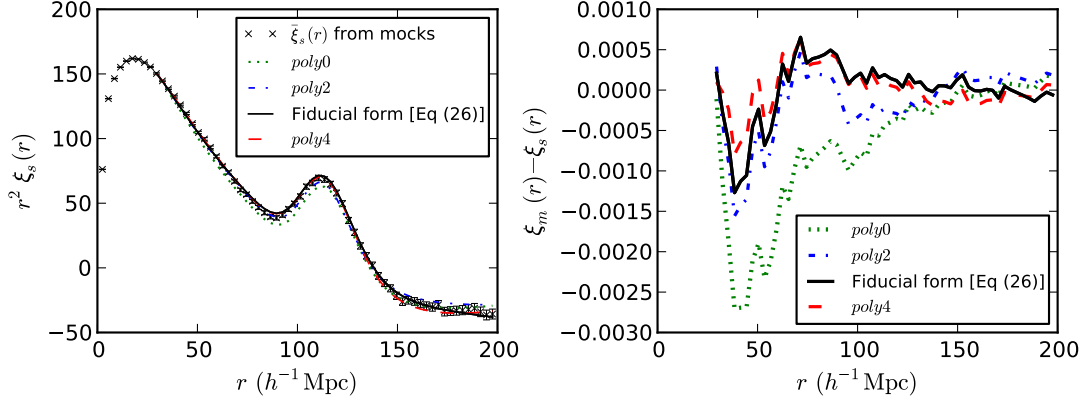


Figure 4. (left) Fits to the average redshift-space correlation function of the mocks (black crosses) using Equation (25) with $A(r)$ being *poly0* (dotted green line), *poly2* (dash-dotted blue line), fiducial form (Equation (26)) (solid black line) and *poly4* (dashed red line). (right) The corresponding residuals of the fits (note that the fitting range is $30 < r < 2000 h^{-1}$ Mpc). One can see that the fit using the fiducial form matches the data better than the fits with *poly0* and *poly2*. However, the improvement between the fiducial form and *poly4* is negligible as reflected by the similar shapes of the solid and dashed curves. These results motivate our choice of $A(r)$ given in Equation (26). We have also allowed Σ_{nl} to vary in these fits. Using the fiducial form, we find $\Sigma_{nl} = 8.1 h^{-1}$ Mpc, which is close to the value we assumed in deriving the covariance matrix.

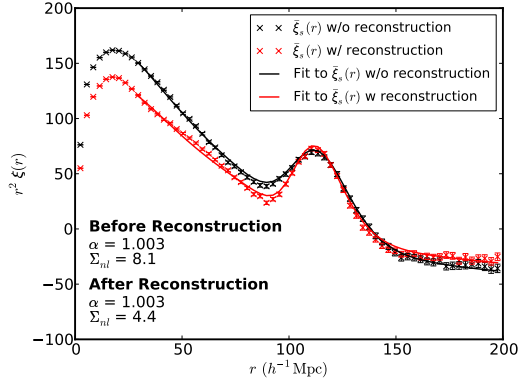


Figure 5. Fits to the average of the mock redshift-space correlation functions before and after reconstruction. The black crosses are the mock data before reconstruction and the black line is its best-fit model. The red crosses are the mock data after reconstruction and the red line is its best-fit model. We have allowed Σ_{nl} to vary in these fits, the results are summarized on the plot. We find that before reconstruction, the shift in the acoustic peak is already very small ($\alpha \sim 1$), so we do not expect reconstruction to shift the peak much closer to its predicted linear theory position. However, we find that Σ_{nl} was reduced by a factor of 1.8 after reconstruction, indicating that reconstruction was able to mitigate the acoustic peak smearing due to non-linear structure growth.

4 LASDAMAS REDSHIFT SPACE RESULTS

4.1 Without Reconstruction

We begin by studying the LasDamas mocks in redshift space without reconstruction. We perform our fits on the mocks using the fiducial model and fitting techniques outlined in the previous section and find that a few of the mocks do not give compelling measurements of α due to their relatively weak acoustic features. We attempt to identify which mocks have poorly constrained values of α by performing our fits

at different test values of α_i using our fiducial model and measuring the resulting χ^2 . This allows us to calculate

$$p(\alpha_i) = \frac{e^{-\chi^2(\alpha_i)/2}}{\sum_j e^{-\chi^2(\alpha_j)/2} \Delta\alpha}, \quad (30)$$

the probability of measuring the acoustic scale to be $\alpha = \alpha_i$ from a particular mock. Here, the denominator is a normalization factor equivalent to integrating over all test values of α where $\Delta\alpha$ is the difference between the test values. We calculate a mean and a standard deviation for our $p(\alpha)$ distributions as

$$\langle \alpha \rangle = \sum_i \alpha_i p(\alpha_i) \Delta\alpha \quad (31)$$

$$\sigma_\alpha = \sqrt{\sum_i [\alpha_i - \langle \alpha \rangle]^2 p(\alpha_i) \Delta\alpha}. \quad (32)$$

A small standard deviation indicates that the best-fit α measured from the mock is well constrained. Conversely, a large standard deviation indicates that it is difficult to measure an accurate value of α from the mock.

In Figure 6, we have plotted the fit results using the fiducial model for 2 of our mock redshift-space correlation functions, $\xi_s(r)$, that appear to have well constrained values of α (upper 2 panels) and 2 that do not (lower 2 panels). These are representative of the other well and poorly constrained mocks in our set. For a detailed description of the information plotted, please see the figure caption.

The left column in each set shows the actual fit to the mock correlation function using the fiducial model. The best-fit values of α and their corresponding minimum χ^2/dof are given on the plots. In comparing the well constrained mocks to the poorly constrained mocks, we can see that in order to obtain a fairly certain measurement of best-fit α , the mock must have a prominent acoustic peak. If one ignores the best-fit models which can be used to guide the eye, the acoustic features in both of the poorly constrained mocks are much weaker than in the well constrained mocks.

The middle column in each set shows the $\Delta\chi^2 =$

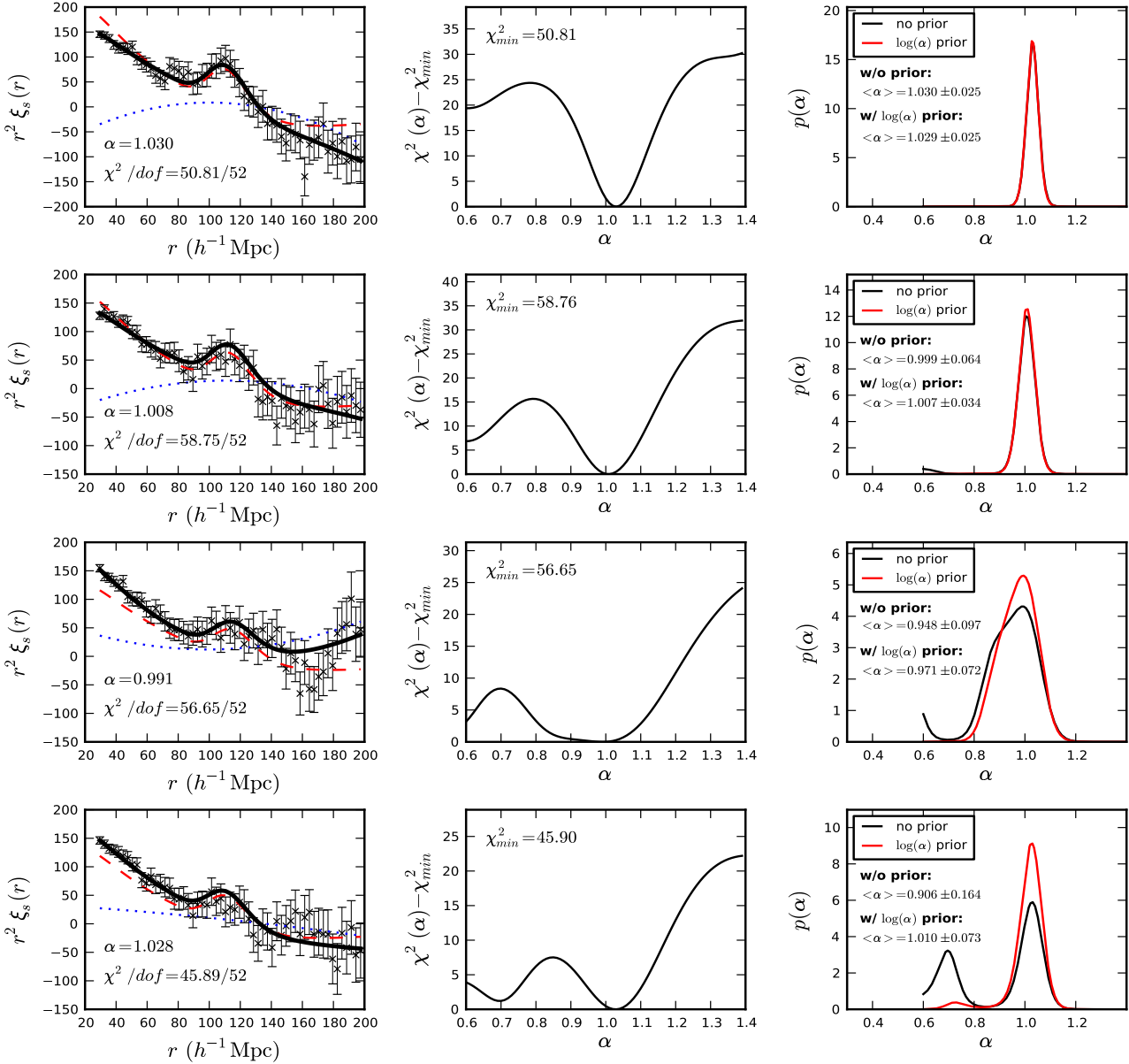


Figure 6. Sample fit results from the fiducial model for our redshift-space mocks, $\xi_s(r)$. (rows 1+2) Results from mocks that have well constrained measures of α . (rows 3+4) Results from mocks that have poorly constrained measures of α . (left column) Actual fits using the fiducial model. The model (black line) is overlotted on the mock data (black crosses with error bars). The dotted blue line corresponds to the $A(r)$ term in the model and the dashed red line corresponds to the $B^2\xi_m(\alpha r)$ term. Comparing rows 1 & 2 with rows 3 & 4 suggests that there must be a fairly prominent acoustic peak in order to obtain a well constrained measurement of α . (middle column) The $\Delta\chi^2 = \chi^2(\alpha) - \chi_{min}^2$ curve. The large differences in χ^2 between the minimum and the plateaus of the well constrained cases indicate that we have robust detections of the χ^2 minimum and hence the best-fit α which corresponds to this minimum. In the poorly constrained mocks, the difference is much smaller and there may be double minima at small $\Delta\chi^2$ from each other, indicating a poor detection of the best-fit α . (right column) The $p(\alpha)$ distribution versus α (black line) calculated from $\chi^2(\alpha)$, Equation (30). The red line is the same curve but with a 15% Gaussian prior on $\log(\alpha)$. We say best-fit α is well constrained in a mock, when the standard deviation of the $p(\alpha)$ distribution is small, and not well constrained when the standard deviation is large, even after the prior is applied. In some mocks, we see significant χ^2 differences between the minimum and the plateau, however, the σ_α measured may still be large. This is due to a downturn in the $\chi^2(\alpha)$ curve at $\alpha \sim 0.7$ (see the second row). Such a downturn is not physically motivated because it is caused by the model attempting to hide the acoustic peak in the larger errors at large r . Hence, we introduce the prior on $\log(\alpha)$ to suppress this effect.

$\chi^2(\alpha) - \chi_{min}^2$ curve for each mock. The $\chi^2(\alpha)$ here is the same as that which appears in Equation (30) and χ_{min}^2 is the minimum of $\chi^2(\alpha)$, i.e. χ^2 at the best-fit value of α . One can see that for the well constrained mocks, the curve is nearly parabolic around the minimum (expected if α is Gaussian distributed) and then plateaus at extreme values of α . The height in $\Delta\chi^2$ of these plateaus can be used as a proxy for the significance of the χ^2 minimum. In the poorly constrained mocks, the plateau occurs at much smaller $\Delta\chi^2$ values. In addition, there may be double minima at small differences in χ^2 . These indicate that we are not detecting the χ^2 minimum (and hence best-fit α) robustly.

In the right panels, we use these $\chi^2(\alpha)$ curves to calculate their corresponding $p(\alpha)$ distributions using Equation (30). These are plotted as the black lines. The red lines include an additional 15% Gaussian prior on $\log(\alpha)$, i.e. $\chi^2(\alpha) \rightarrow \chi^2(\alpha) + \left(\frac{\log(\alpha)}{0.15}\right)^2$. We apply this weak prior because in some of the cases where the best-fit α should be well constrained, i.e. in the second row where the $\Delta\chi^2$ curve is nicely parabolic around a minimum that is at a significant $\Delta\chi^2 \sim 15$ away from the plateau, we still measure a large σ_α from the $p(\alpha)$ distribution. This is due to a slight downturn in the χ^2 versus α curve (and hence an upturn in the $p(\alpha)$ distribution) at $\alpha \sim 0.7$. At these small α , the acoustic peak in the model is getting pushed out to large r . Here, the error bars are larger so the fitter is having an easier time hiding the acoustic peak in the errors. Since this downturn in χ^2 is not physically motivated, we apply this prior to downweight the χ^2 values at extreme α . One can see the effectiveness of the prior by noticing that the upturn in $p(\alpha)$ disappears after the prior is applied to the mock in the second row.

As mentioned previously, the acoustic scale is well constrained in the mocks that have very small standard deviations in α . In these cases, the inferred standard deviation can become even smaller after the prior is applied, not due to any dramatic change in the general shape of the curve but rather because the tails become suppressed by the prior. The mocks where α is not well constrained, however, have very broad distributions with large standard deviations even after a prior is applied. This suggests that we may segregate the well constrained mocks from the poorly constrained mocks by setting a cutoff in the standard deviation after applying the prior on $\log(\alpha)$. We also note here that, after applying the prior, the mean α of the $p(\alpha)$ distribution should be fairly close to the best-fit α from the fiducial model for the well constrained mocks. This is indeed what we observe. Any discrepancy is likely due to the fact that the $p(\alpha)$ distribution is not exactly Gaussian.

A plot of the standard deviations versus the best-fit α values from the fiducial model are shown in Figure 7. The median of the standard deviations is indicated by the solid grey line and the 98th, 84th, 16th and 2nd percentile levels are indicated by the dashed grey lines. We see that the poorly constrained mocks mostly lie at standard deviations larger than 7% (indicated by the black horizontal line in the plot). Hence, we make a cutoff in standard deviation at 7% and take all mocks that lie above this cutoff to have poorly constrained measurements of α (circled in black). Both of the poorly constrained mocks shown in Figure 6 fall into this category. For our redshift-space mocks before reconstruction, we find that 8 ($\sim 4\%$) have fairly poor mea-

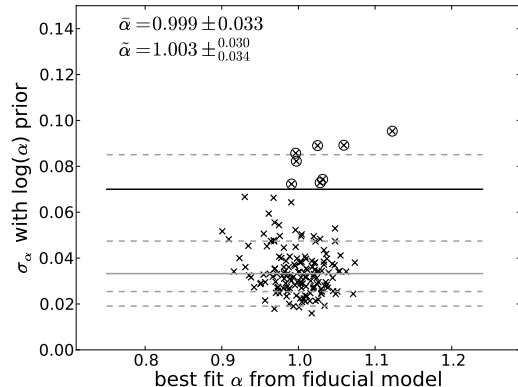


Figure 7. The standard deviations of $p(\alpha)$ for the redshift-space mocks plotted against their best-fit α values measured using the fiducial model. A large standard deviation indicates that α is poorly constrained in its corresponding mock. The solid grey line indicates the median of the standard deviations while the dashed grey lines indicate the 98th, 84th, 16th and 2nd percentiles. We see that most of these poorly constrained mocks fall above a standard deviation of 7%. Hence we impose a 7% cutoff (black horizontal line) in standard deviation and remove all the mocks with standard deviations above this cutoff from our fitting sample. The mocks with uncertain α measurements based on this metric are circled. There are 8 of such mocks, which is $\sim 4\%$ of our sample. The mean and median values of best-fit α measured using the fiducial model after removing the poorly constrained mocks are listed on the plot.

surements of α . The mean and median values of the best-fit α from the fiducial model are given in the plot after removing the poorly constrained mocks. We use this procedure to remove these poorly constrained mocks from our α -fitting sample before proceeding. Note that they are still included in our covariance matrix derivation.

To verify the robustness of our covariance modeling and the fiducial model, we compare the α values we measure from the fiducial model to those we measure when the fiducial model parameters are slightly changed or if we fit using a different covariance matrix. A summary of the results of these fits, after removing the poorly constrained mocks as just described, can be found in Table 2. We quote the mean of any quantity x and its standard deviation as \bar{x} and we quote the median with the 84th/16th percentiles as \tilde{x} throughout this paper. For the fiducial model, we find $\bar{\alpha} = 0.999 \pm 0.033$ and $\tilde{\alpha} = 1.003 \pm_{0.034}^{0.030}$. This means that we can measure the shift in the acoustic scale to about 3-3.5% accuracy from our mocks before reconstruction.

Our first test is to see whether we can recover the true acoustic scale using our fiducial model but with $P_m(k)$ derived from slightly different cosmologies to that used by LasDamas. Figure 8 shows the α values derived from these incorrect cosmologies versus the α values obtained through fits using the fiducial model (i.e. with the correct cosmology). The α values obtained from the incorrect cosmologies have been scaled to the correct cosmology where necessary by multiplying the ratio of the sound horizons, $r_{s,\text{lin}}(\text{correct})/r_{s,\text{lin}}(\text{incorrect})$, where the $r_{s,\text{lin}}$ are calculated using Equation (6) in Eisenstein & Hu (1998). For a more detailed discussion of the sound horizon calculation, please refer to Paper III. The figure caption gives an ex-

Table 2. Redshift space fitting results for various models

Model	$\bar{\alpha}$	$\tilde{\alpha}$	$\overline{\Delta\alpha}^1$	$\widetilde{\Delta\alpha}$	$\overline{\chi^2/dof}$
Redshift Space without Reconstruction					
Fiducial [f]	0.999 ± 0.033	$1.003 \pm_{0.034}^{0.030}$	–	–	52.96/52
Fit with 15% larger Ω_m using fiducial $A(r)$. ²	0.998 ± 0.034	$1.001 \pm_{0.035}^{0.029}$	-0.002 ± 0.002	$-0.001 \pm_{0.002}^{0.001}$	53.29/52
Fit with $n_s = 0.96$ using fiducial $A(r)$.	1.001 ± 0.033	$1.004 \pm_{0.034}^{0.030}$	0.002 ± 0.001	$0.001 \pm_{0.001}^{0.001}$	52.92/52
Fit with $N_{rel} = 4$ using fiducial $A(r)$.	1.006 ± 0.033	$1.008 \pm_{0.033}^{0.032}$	0.007 ± 0.005	$0.006 \pm_{0.001}^{0.001}$	52.85/52
Fit with $\Sigma_{nl} \rightarrow 0$.	0.996 ± 0.036	$0.997 \pm_{0.032}^{0.032}$	-0.003 ± 0.020	$-0.004 \pm_{0.013}^{0.013}$	54.29/52
Fit with $\Sigma_{nl} \rightarrow \Sigma_{nl} + 2$.	1.001 ± 0.034	$1.005 \pm_{0.034}^{0.028}$	0.002 ± 0.005	$0.002 \pm_{0.005}^{0.004}$	53.28/52
Fit with <i>poly0</i> .	0.995 ± 0.035	$0.996 \pm_{0.030}^{0.034}$	-0.004 ± 0.012	$-0.003 \pm_{0.008}^{0.007}$	56.03/55
Fit with <i>poly2</i> .	0.997 ± 0.033	$1.002 \pm_{0.035}^{0.030}$	-0.002 ± 0.004	$-0.001 \pm_{0.003}^{0.002}$	54.44/53
Fit with <i>poly4</i> .	0.999 ± 0.033	$1.002 \pm_{0.033}^{0.031}$	0.000 ± 0.001	$0.000 \pm_{0.000}^{0.000}$	51.81/51
Fit with $50 < r < 200h^{-1}$ Mpc fitting range.	1.000 ± 0.033	$1.004 \pm_{0.033}^{0.030}$	0.001 ± 0.005	$0.001 \pm_{0.003}^{0.003}$	45.73/45
Fit with $20 < r < 200h^{-1}$ Mpc fitting range.	1.002 ± 0.033	$1.004 \pm_{0.033}^{0.033}$	0.003 ± 0.008	$0.003 \pm_{0.006}^{0.006}$	59.45/57
Fit with $70 < r < 150h^{-1}$ Mpc fitting range.	0.999 ± 0.033	$1.001 \pm_{0.031}^{0.033}$	0.000 ± 0.010	$-0.000 \pm_{0.008}^{0.009}$	21.83/22
Fit using mock covariance matrix.	1.002 ± 0.027	$1.003 \pm_{0.026}^{0.025}$	0.003 ± 0.022	$0.003 \pm_{0.017}^{0.018}$	52.80/52
Redshift Space with Reconstruction					
Fiducial [f]	1.001 ± 0.021	$1.001 \pm_{0.022}^{0.020}$	–	–	53.69/52
Fit with 15% larger Ω_m using fiducial $A(r)$. ²	1.001 ± 0.021	$1.001 \pm_{0.022}^{0.020}$	-0.000 ± 0.001	$-0.000 \pm_{0.001}^{0.001}$	51.86/52
Fit with $n_s = 0.96$ using fiducial $A(r)$.	1.002 ± 0.021	$1.002 \pm_{0.022}^{0.020}$	0.001 ± 0.000	$0.001 \pm_{0.000}^{0.000}$	51.84/52
Fit with $N_{rel} = 4$ using fiducial $A(r)$.	1.006 ± 0.021	$1.006 \pm_{0.022}^{0.020}$	0.005 ± 0.001	$0.005 \pm_{0.001}^{0.001}$	51.95/52
Fit with $\Sigma_{nl} \rightarrow 0$.	1.001 ± 0.022	$1.001 \pm_{0.020}^{0.022}$	-0.000 ± 0.004	$-0.001 \pm_{0.003}^{0.004}$	53.83/52
Fit with $\Sigma_{nl} \rightarrow \Sigma_{nl} + 2$.	1.002 ± 0.021	$1.001 \pm_{0.020}^{0.022}$	0.001 ± 0.004	$0.001 \pm_{0.004}^{0.002}$	53.99/52
Fit with <i>poly0</i> .	1.000 ± 0.021	$1.000 \pm_{0.020}^{0.019}$	-0.002 ± 0.004	$-0.001 \pm_{0.004}^{0.004}$	57.34/55
Fit with <i>poly2</i> .	1.000 ± 0.021	$1.001 \pm_{0.022}^{0.021}$	-0.001 ± 0.002	$-0.001 \pm_{0.001}^{0.001}$	55.41/53
Fit with <i>poly4</i> .	1.001 ± 0.021	$1.001 \pm_{0.022}^{0.021}$	-0.000 ± 0.000	$-0.000 \pm_{0.000}^{0.000}$	52.68/51
Fit with $50 < r < 200h^{-1}$ Mpc fitting range.	1.001 ± 0.021	$1.000 \pm_{0.021}^{0.023}$	0.000 ± 0.002	$0.000 \pm_{0.002}^{0.001}$	46.58/45
Fit with $20 < r < 200h^{-1}$ Mpc fitting range.	1.005 ± 0.021	$1.004 \pm_{0.020}^{0.022}$	0.004 ± 0.003	$0.004 \pm_{0.003}^{0.003}$	60.06/57
Fit with $70 < r < 150h^{-1}$ Mpc fitting range.	1.001 ± 0.026	$1.003 \pm_{0.019}^{0.022}$	-0.000 ± 0.012	$0.000 \pm_{0.005}^{0.004}$	22.69/22
Fit using mock covariance matrix.	1.004 ± 0.017	$1.003 \pm_{0.014}^{0.017}$	0.003 ± 0.015	$0.001 \pm_{0.010}^{0.015}$	54.22/52

¹ $\Delta\alpha = \alpha_{[i]} - \alpha_{[f]}$, where i is the model number.

² We scale the measured sound horizons to the LasDamas cosmology where necessary.

explicit description of the items plotted. Note that we define $\Delta\alpha \equiv \alpha_{y\text{-axis}} - \alpha_{x\text{-axis}}$, where we always have $\alpha_{x\text{-axis}}$ equal to the values of α measured using the fiducial model.

The top left panel shows the α values from a fit using $A(r) = 0$ (i.e. *poly0*) and a cosmology with a 15% larger value of Ω_m (and hence Ω_b). This difference should give rise to an acoustic scale that is about 5% smaller. The top right panel shows the results from the same fit with the fiducial $A(r)$ form instead of *poly0*. We expect the mean and median $\Delta\alpha$ values to be ~ 0 if we can recover the true acoustic scale using an incorrect cosmology template (i.e. if the α values plotted on the 2 axes are perfectly correlated). We see that this result is recovered with $\sim 0.2\%$ scatter when we fit using the fiducial $A(r)$ form. This is $\sim 1\%$ smaller than the scatter found when fitting with *poly0*, another indication of the advantages of fitting with a non-zero $A(r)$.

The middle left panel of Figure 8 shows the α values from fits using *poly0* and a cosmology with $n_s = 0.96$ plotted against the results from the fiducial model ($n_s = 1.0$). The difference in n_s should not affect the position of the acoustic scale, but only the shape of the model. The analogous results using the fiducial $A(r)$ form instead of *poly0* are shown in the middle right. The correct acoustic scale is recovered with $\Delta\alpha$ very close to 0 and $\sim 0.1\%$ scatter when the fiducial $A(r)$ form is used. The corresponding *poly0* fit does a poorer job with a scatter in $\Delta\alpha \sim 0$ of about 1%. Overall, the fiducial model seems to be able to recover the true acoustic scale even if its power spectrum template has a slightly different cosmology. This and the previous example show how important it is to fit with a non-zero $A(r)$ term if we are not certain of the true model cosmology to be used (i.e. in the case of actual observations).

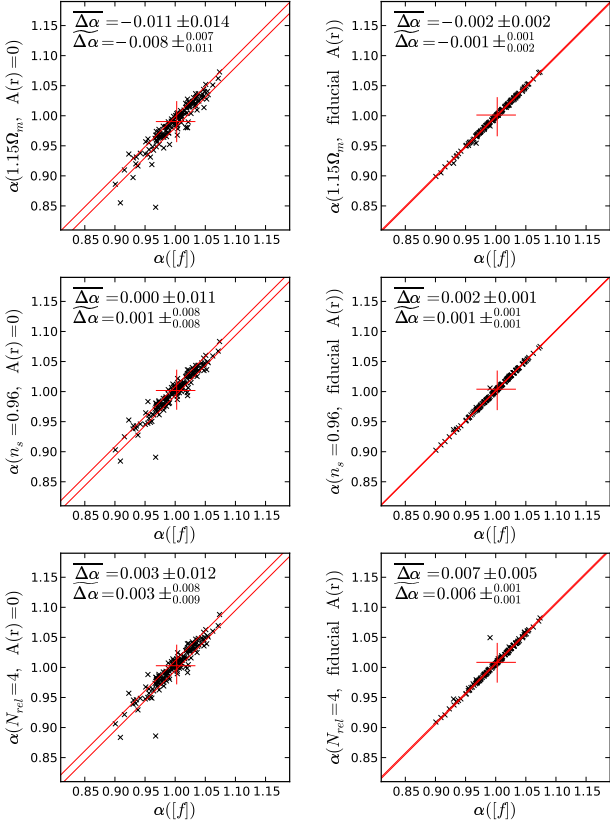


Figure 8. Validation of our fitting method using LasDamas mocks: varying template cosmology. Here we have plotted the redshift-space α values measured using the fiducial model (i.e. using the true LasDamas cosmology) on the x -axis versus the α values measured using templates derived from slightly different cosmologies on the y -axis. For the incorrect cosmology templates, we have performed the fits using *poly0* (left) and the fiducial $A(r)$ form (right). The α values from the incorrect cosmologies have been scaled to the correct cosmology where necessary. The red cross indicates the median α values with their 16th and 84th percentiles. The red lines indicate the 16th and 84th percentiles of $\Delta\alpha = \alpha_{y\text{-axis}} - \alpha_{x\text{-axis}}$. These values are given in the plots. Overall, we see that the fiducial $A(r)$ form is better at recovering the correct acoustic scale than *poly0* and that our fiducial model is robust in recovering the correct acoustic scale even when the template power spectrum is derived from a slightly different cosmology. (top) Results when we fit with a template cosmology where Ω_m is 15% higher than LasDamas. (middle) Results when we fit with a template cosmology where $n_s = 0.96$. (bottom) Results when we fit with a template where there are 4 relativistic neutrino species. We see that the $\Delta\alpha$ offset is larger in this case, especially when fitting with the fiducial $A(r)$ form. This $\sim 0.6\%$ offset is likely a result of the template BAO shape deviating slightly from that in the mock data.

The y -axis of the bottom panels in Figure 8 correspond to α values measured using *poly0* (left) and fiducial $A(r)$ (right) with a template cosmology consisting of 4 relativistic neutrino species ($N_{rel} = 4$) instead of the standard 3. We use the same Ω_m , $\Omega_b h^2$, and epoch of matter-radiation equality as the $N_{rel} = 3$ case, so that the rough shape of the power spectrum is preserved. This requires $H_0 = 74.3$ km/s/Mpc. As in the previous cases, the scatter in $\Delta\alpha$ is smaller if we employ the fiducial $A(r)$ rather than *poly0*. However, we

find a mean offset of 0.6% when using an $N_{rel} = 4$ template, after scaling by the appropriate sound horizon. We believe this is because the shape of the template around the BAO feature is slightly different from the $N_{rel} = 3$ case, e.g., because the baryon fraction in this model is different. While the 0.6% offset is much smaller than the statistical errors of the DR7 data set, larger surveys might need to iterate their fits to converge to a sufficiently accurate template when investigating variations in the number of relativistic species.

Next we test how changing the value of Σ_{nl} in $P_m(k)$ of the fiducial model affects the measured acoustic peak position. In the top left panel of Figure 9, we plot the α values measured using fits with $\Sigma_{nl} = 10h^{-1}$ Mpc versus those derived from the fiducial model ($\Sigma_{nl} = 8h^{-1}$ Mpc) in redshift space. One can see a tight correlation between the 2 sets of α with consistent mean and median values. The mean and median $\Delta\alpha$ values are consistent with 0 and only have $\sim 0.5\%$ scatter. The top right panel shows the corresponding χ^2 values from the fits. The number of degrees of freedom is calculated by subtracting the number of fitting parameters (5 in our fiducial form: B^2 , a_1 , a_2 , a_3 and α) from the number of data points being fit (57 for our fiducial fitting range of $30 < r < 200h^{-1}$ Mpc). The tight correlation in α and the very small change in χ^2/dof between the 2 models suggest that the value of α is not sensitive to small changes in Σ_{nl} . However, if we use a less sensible value of Σ_{nl} like $\Sigma_{nl} = 0h^{-1}$ Mpc which corresponds to no acoustic peak smearing (very unlikely, especially before reconstruction), $\Delta\alpha$ is still consistent with 0 but the scatter increases to 1 – 2%. This suggests that the fiducial form defined by Equations (25 & 26) returns consistent values of α as long as a reasonable value of Σ_{nl} is used.

The left panel of the 2nd row in Figure 9 shows the α values measured from fits using an $A(r)$ that is an order higher than the fiducial form (i.e. *poly4*) versus the α values measured using the fiducial model. Again, a tight correlation exists between the 2 sets of α with the mean and median values agreeing nicely. The mean and median values of $\Delta\alpha$ are consistent with 0 and have negligible scatter. The right panel in the 2nd row shows the analogous plot for the χ^2 values. One can see that the average χ^2 decreases by ~ 1 as one expects when increasing the number of nuisance parameters by 1. This suggests that continuing to increase the order of $A(r)$ beyond that in the fiducial model offers little improvement to the fits. However, as long as one does not increase the order to a point where noise in the data is being fit, one should measure consistent values of α . When $A(r)$ is taken to be an order less than fiducial (i.e. *poly2*), the scatter goes up slightly to $\sim 0.3\%$ and when *poly0* is used, the scatter increases to $\sim 1\%$. Hence, decreasing the order of $A(r)$ is feasible, but decreasing the order by too much will give a less consistent measurement of α .

Finally we test how adjusting the fitting range affects our measurements of α . Changing the minimum of the fitting range from $30h^{-1}$ Mpc (fiducial) to $50h^{-1}$ Mpc seems to have little effect on α . The 3rd row of Figure 9 shows the α and χ^2 values obtained using these 2 fitting ranges. One can see that the mean and median α values agree nicely and that the 2 sets of α values are obviously correlated. $\Delta\alpha$ is again consistent with 0 and has very small scatter ($\sim 0.4\%$). The χ^2 values decreased by about 7 on average, which is expected since the number of data points fit decreased by 7.

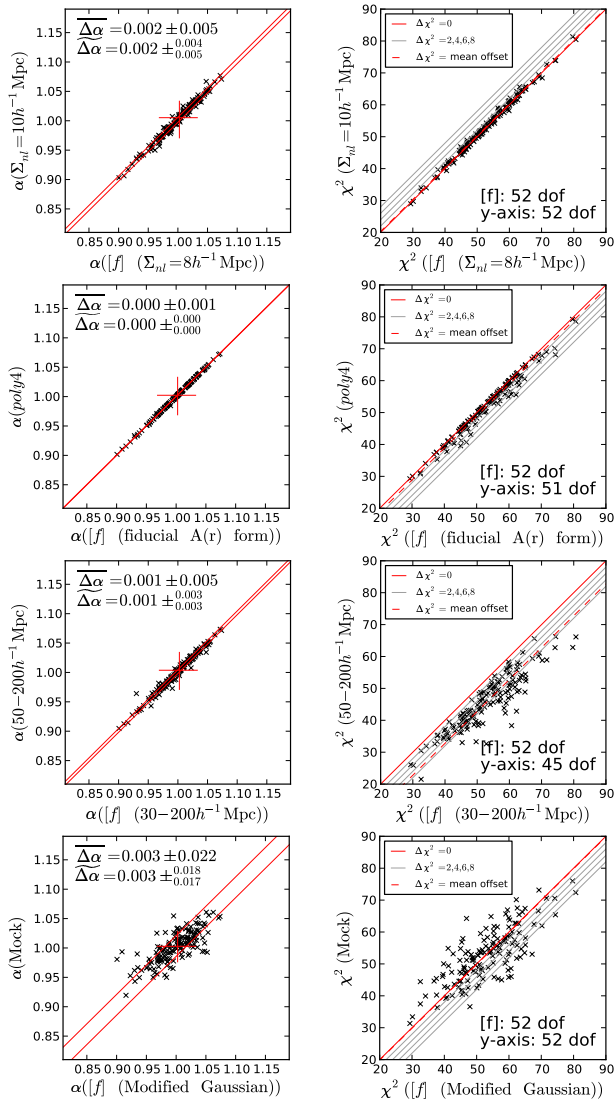


Figure 9. Validation of our fitting method using LasDamas mocks: varying fitting/model parameters. This figure is akin to Figure 8 in that the left panels show similar plots of redshift-space α values measured using the fiducial model (x -axis) versus those measured using models in which the fiducial parameters are slightly tweaked (y -axis). However, instead of varying the template cosmology, here we vary other fiducial model parameters such as Σ_{nl} (top), the order of $A(r)$ (2nd row) and the fitting range (3rd row). The tight correlations shown in all of these plots indicate the robustness of our covariance matrix estimators and the robustness of our fiducial model to small changes in model parameters. The right panels show corresponding plots of the measured best-fit χ^2 values. In all cases we see that the χ^2 values shift by reasonable amounts given the addition or subtraction of degrees-of-freedom as we change the fiducial parameters. (top) Results when we fit using $\Sigma_{nl} = 10h^{-1}$ Mpc. (2nd row) Results when we fit using $poly4$. (3rd row) Results when we use a fitting range of $50 < r < 200h^{-1}$ Mpc. (bottom) For completeness, we show the comparison between fits using the mock covariance matrix (Equation (3)) and fits using the MGCM. A correlation between the 2 sets of α can be seen, but the noisiness of the mock covariance matrix is responsible for the larger scatter. Similarly, the corresponding χ^2 plot shows a fair bit of scatter. However, the average χ^2 values obtained using these 2 different covariance matrices match nicely.

We perform similar experiments by shifting the fitting range to $20 < r < 200h^{-1}$ Mpc and $70 < r < 150h^{-1}$ Mpc. In both cases, $\Delta\alpha = 0$ lies within slightly larger scatter ($\sim 0.7-1\%$). In the prior case, this is likely due to non-linear effects at small scales coming into play. These effects are not well modeled by our fitting template. In the latter case, the larger scatter is likely caused by some of the acoustic information being cut out by using such a small fitting range.

For completeness, we also show the α values obtained through using the mock covariance matrix (Equation (3)) versus those obtained using the MGCM and the fiducial model. Since the mock covariance matrix is noisy, we expect there to be significant scatter in the α versus α and χ^2 versus χ^2 plots. These are shown in the bottom panels of Figure 9. A correlation between the two α sets is still visible, but it is not as tight as those in the upper panels. $\Delta\alpha$ is still consistent with 0 but the scatter is now $\sim 2\%$. Note that the average χ^2 values of the 2 cases match well. This indicates that the MGCM is a reasonable approximation to the covariances we expect in our mock data.

4.2 With Reconstruction

Next we study the LasDamas mocks in redshift space after reconstruction. We find that after reconstruction, our ability to constrain the acoustic scale in each individual mock as measured by the standard deviation of α is greatly improved. We plot σ_α before reconstruction against those after reconstruction in Figure 11. The black diagonal line is the 1-1 line. One can see that only a few of the mocks have larger standard deviations after reconstruction but they are not much larger. Most of the points lie significantly below the line with the median change in σ_α equal to 1.1% as indicated on the plot. Hence, in general, reconstruction can significantly improve our ability to constrain α .

One can also see that after reconstruction, there are no longer any poorly constrained mocks that lie above the 7% cutoff (black horizontal line) imposed in the unreconstructed case. The solid grey line indicates the mean σ_α after reconstruction and the dashed grey lines correspond to the 98th, 84th, 16th and 2nd percentiles, similar to Figure 7 for redshift space without reconstruction.

As we saw in §4.1, the mocks where α is well constrained have strong acoustic features. Figure 11 showed that in reconstructed redshift space our measurements of best-fit α should be much more reliable. This implies that the acoustic peak in the poorly constrained mocks from before should be more prominent after reconstruction as we would expect. In Figure 10, we show the same 2 poorly constrained mocks as in Figure 6. The fit results from both of these mocks clearly demonstrate how effective reconstruction is. The acoustic peaks can be clearly seen now and the χ^2 minima corresponding to the best-fit α values are significantly different from the plateau values. The $p(\alpha)$ curves have also become more Gaussian in shape with standard deviations much smaller than before (by factors of ~ 1.9 and ~ 2.5 respectively). These are characteristic of the improvements seen for the other mocks which were poorly constrained before reconstruction.

In Figure 12, we have plotted the distribution of $(\alpha_{bf} - \bar{\alpha})/\sigma_\alpha$ which is a proxy for the signal-to-noise of our α measurement. Here, α_{bf} is the best-fit value of α for each mock

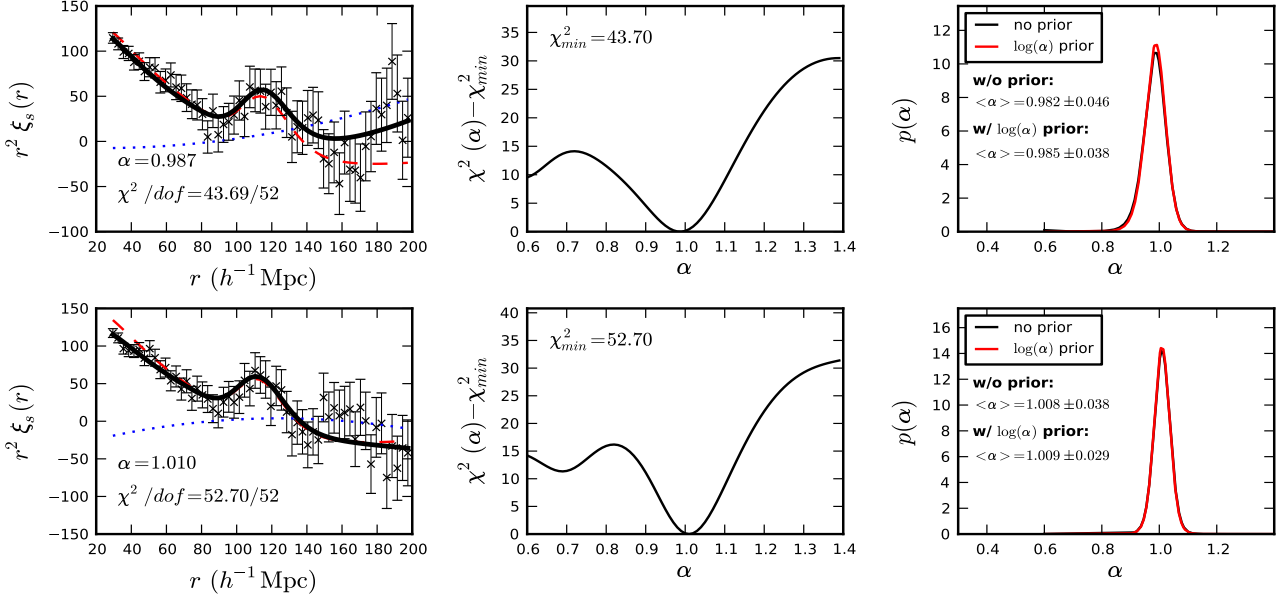


Figure 10. The same poorly constrained mocks as in Figure 6 after reconstruction. One can see that reconstruction has improved our ability to obtain a solid measurement of α in both cases. The acoustic peaks are now clearly visible, there are significant differences in χ^2 between the minima of the $\Delta\chi^2$ curves and the plateaus, and the $p(\alpha)$ distributions are now regular Gaussians with standard deviations ~ 1.9 and ~ 2.5 times smaller than before reconstruction. This type of improvement is characteristic of the other previously poorly constrained mocks in our sample and again emphasizes the utility of reconstruction.

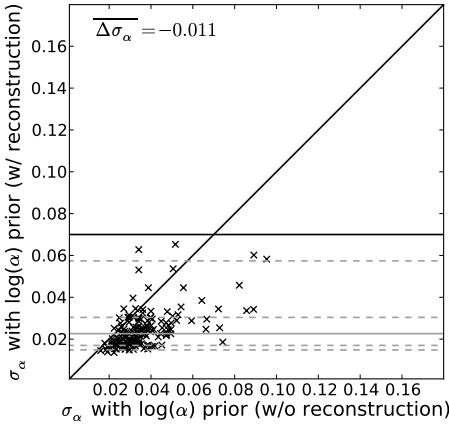


Figure 11. The standard deviations of $p(\alpha)$ for each mock before reconstruction versus those after reconstruction. The diagonal black line is a 1-1 line to guide the eye. Only a few of the mocks have slightly larger standard deviations after reconstruction, most of the mocks lie very much below the diagonal line. The median change in standard deviation is 1.1% which implies that our ability to constrain α increases significantly after reconstruction. Note that also, after reconstruction, there are no longer any poorly constrained mocks with standard deviations larger than 7% (black horizontal line), the cutoff imposed in Figure 7. The grey solid and dashed lines are as in Figure 7.

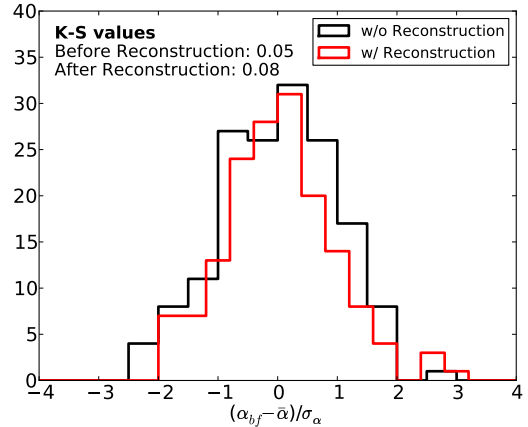


Figure 12. The distributions of $(\alpha_{bf} - \bar{\alpha})/\sigma_\alpha$ before (black) and after (red) reconstruction, where α_{bf} is the best-fit value of α for each mock and $\bar{\alpha}$ is the mean of the best-fit values. This is a good measure of the signal-to-noise ratio of our best-fit α values. Both distributions are nearly Gaussian as indicated by the K-S values shown in the plot. The Gaussianity of these distributions implies that the σ_α values measured from $p(\alpha)$ are representative estimates of the error on α for each mock.

and $\bar{\alpha}$ is the mean of the best-fit values. The distribution before reconstruction is shown in black and the distribution after reconstruction is shown in red. One can see that both distributions are roughly Gaussian. A standard K-S test gives a value of ~ 0.05 before reconstruction and ~ 0.08

after reconstruction in comparison to a Gaussian distribution (recall that a value close to 0 indicates a better match to the normal distribution). This demonstrates that the standard deviations of $p(\alpha)$ are a representative estimate of the errors on the best-fit values of α for each mock.

Next, we again tweak the fiducial model parameters slightly and test the robustness of our fitting form and our covariance matrix. The results of the fits are summarized in

Table 2 and in Figure 14. This figure is essentially analogous to Figure 8 and Figure 9, however, we have replaced the scatter plots with histograms of $\Delta\alpha = \alpha_{[i]} - \alpha_{[f]}$. Here, $\alpha_{[i]}$ are the slightly tweaked models as indicated by the titles. The fiducial model has mean $\bar{\alpha}_{[f]} = 1.001 \pm 0.021$ and median $\tilde{\alpha}_{[f]} = 1.001 \pm_{0.022}^{0.020}$ (recall that before reconstruction these were $\bar{\alpha} = 0.999 \pm 0.033$ and $\tilde{\alpha} = 1.003 \pm_{0.034}^{0.030}$). This indicates that the error on the acoustic scale decreased by about a factor of 1.6 after reconstruction. We know that $V \propto \sigma^{-2}$, where V is the survey volume required to achieve a variance σ^2 . Therefore, we would have to increase the survey volume by ~ 2.5 times to achieve this same factor of 1.6 decrease in the error. Also, note that in general, the scatters in the mean and median α and $\Delta\alpha$ values from the various fits are smaller after reconstruction, another indication of its effectiveness.

The various panels of Figure 14 show $\Delta\alpha$ values for different tweaks to the fiducial model. The median values are marked by the red lines (see caption for more details). Further cases are summarized in Table 1. The only case that shows a relatively large scatter in $\Delta\alpha$ is when we fit using the mock covariance matrix instead of the MGCM; this can be attributed to the higher noise in the mock covariance matrix. Also, as in the pre-reconstruction case, we see that for $N_{rel} = 4$, $\Delta\alpha \sim 0.5\%$ which is slightly larger than the other cases. However, in general, $\Delta\alpha \sim 0$ with very small scatter.

It should also be noted here that the cases which had noticeably larger scatter in $\Delta\alpha$ before reconstruction ($\Sigma_{nl} = 0h^{-1}$ Mpc, *poly0* and fitting ranges of $20 < r < 200h^{-1}$ Mpc and $70 < r < 150h^{-1}$ Mpc), no longer do post-reconstruction. This is because reconstruction undoes non-linear structure growth and brings the correlation function closer to its linear theory form (i.e. $\xi_s(r) \rightarrow \xi_m(r)$ and $\Sigma_{nl} \rightarrow 0h^{-1}$ Mpc). The consistency in the measured values of α indicate that after reconstruction, our fiducial model is even more robust against changes in model parameters.

The left panel of Figure 13 shows the α values measured using the WMAP7 cosmology and its MGCM described in §3.2 versus the α values measured using the MGCM for the LasDamas cosmology. One can see that, after rescaling by the ratio of the sound horizons, a perfect correlation exists between the 2 sets of α values. This is also true for the WMAP7 $\pm 1\sigma$ cosmologies shown in Figure 2. The right panel of Figure 13 shows the corresponding values of σ_α measured from $p(\alpha)$. Again, a strong correlation exists and similar trends are observed for the 2 other WMAP7-like cosmologies. Hence, the measurement of the acoustic scale is not affected by the cosmology used for the covariance matrix or the fitting model. This demonstrates the robustness of our fiducial model in dealing with a fitting template constructed using the wrong cosmology as well as our maximum likelihood approach for deriving a suitable covariance matrix for the data.

We conclude this section by demonstrating and comparing the detectabilities of the BAO in the reconstructed (solid red line) and unreconstructed (solid black line) mocks as shown in Figure 15. We have plotted the normalized cumulative distribution of $\Delta\chi^2 = \chi_{BAO}^2 - \chi_{no\ BAO}^2$ for fiducial $A(r)$ (left) and *poly0* (right). Here, the χ^2 values for each mock are calculated by marginalizing over the nuisance parameters only while fixing α at the best-fit value from the

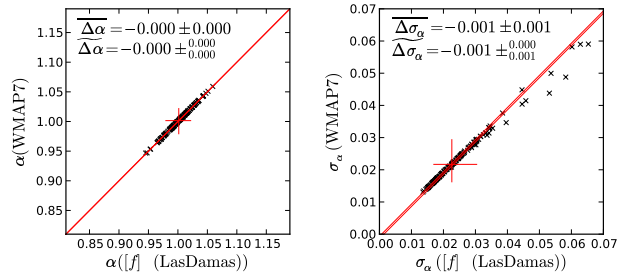


Figure 13. Testing the effects of using the wrong cosmology to derive the covariance matrix and construct the model template. (left) α values measured from the LasDamas mocks in redshift space after reconstruction using a fitting template and MGCM (see Figure 2) based on the WMAP7 cosmology versus those measured using the fiducial model (LasDamas fitting template and its corresponding MGCM). The α values from the WMAP7 cosmology have been rescaled to the LasDamas cosmology. (right) The analogous plot for σ_α measured from $p(\alpha)$. One can see that perfect correlations exist between the axes of both plots. This indicates that our acoustic scale measurements are not affected by deriving the MGCM using the wrong cosmology. Our maximum likelihood method is capable of modifying the matrix from the incorrect cosmology to match that expected from the correct cosmology.

fiducial model or *poly0* fits. χ_{BAO}^2 is the χ^2 obtained in this fashion using a template $\xi_m(r)$ containing BAO. $\chi_{no\ BAO}^2$ is the analogous value obtained using a template that has no BAO feature. While it is true that in the no BAO fits, the value of α we impose may not give the minimum χ^2 , the lack of a BAO feature in the model eliminates its ability to constrain α in these fits. Hence, comparing the BAO and no BAO χ^2 values at the fiducial or *poly0* best-fit α is a reasonable way to circumvent this problem. We obtain the BAO-less model by setting $\Sigma_{nl} = 1000h^{-1}$ Mpc to completely damp out any acoustic signal. This cumulative distribution indicates the fraction of mocks that lie more negative of a given $\Delta\chi^2$ value. Note that we have plotted all 160 mocks here (i.e. we did not throw out any poorly constrained mocks).

If the data favours a model containing BAO, χ_{BAO}^2 should be smaller than $\chi_{no\ BAO}^2$ (i.e. $\Delta\chi^2$ should be negative). The intersections of the dashed horizontal black lines and the distributions correspond to values of $\Delta\chi^2$ that halve the data and hence indicate the median $\Delta\chi^2$ values. One can see that these medians are negative for all cases which indicates that on average the data favours models containing BAO. The median $\Delta\chi^2$ before reconstruction is ~ -10 and after reconstruction, it is ~ -16 for the fits performed using fiducial $A(r)$. The two vertical dashed black lines indicate where $\Delta\chi^2 = 0$ and $\Delta\chi^2 = -9$. The latter corresponds to where a model containing BAO is favoured at 3σ above a model without BAO. Before reconstruction, about 56% of the mocks lie above (more negative of) this 3σ line. After reconstruction, this number increases to 88%. This again indicates that our reconstruction algorithm is helping to restore acoustic information back into the acoustic peak. Hence, the robustness of the BAO detection is further improved by reconstruction.

Although there are some mocks that do not favour a

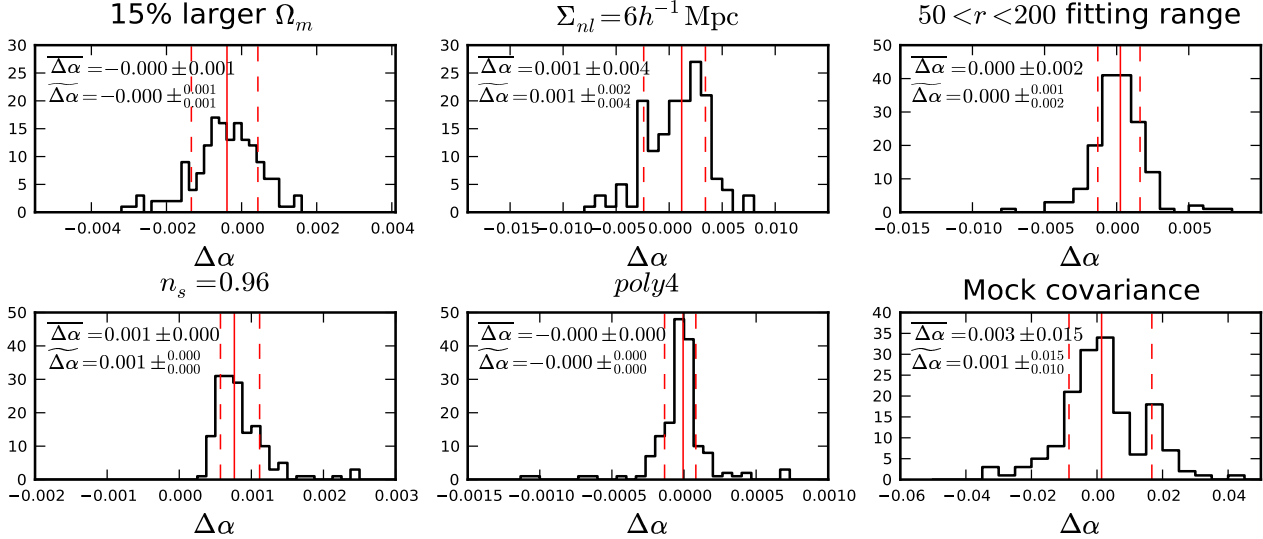


Figure 14. Validation of our fitting method in redshift space after reconstruction using LasDamas mocks. The contents of this figure are comparable to Figures 8 & 9, however, the scatter plots have been replaced by histograms of $\Delta\alpha = \alpha_{[i]} - \alpha_{[f]}$ here. The $\alpha_{[i]}$ are measured from models that are derived by slightly changing the fiducial model parameters. These are indicated above each plot. The solid red lines mark the median $\Delta\alpha$. The dashed red lines indicate the 16th and 84th percentiles. One can see that $\Delta\alpha$ is very close to 0 with small scatter in most of these cases. The slightly larger scatter in the case where we fit using the mock covariance matrix is likely due to the noisiness of that matrix. This indicates that the value of α is insensitive to small changes in template cosmology, Σ_{nl} , order of $A(r)$, fitting range and covariance matrix estimator used. Hence, our basic fitting form and our covariance matrix estimators are robust. The results shown in this figure are all consistent with those found in unreconstructed redshift space.

model with BAO at very high confidence and even a few mocks that do not favour a model with BAO at all ($\Delta\chi^2 > 0$), this does not indicate that we are not detecting the BAO. It is merely a statement that if we take observations of many different regions of the universe, there is a finite chance that the BAO signal will not be robustly detected in some of these regions. This is in contrast to the conclusions drawn in Cabré & Gaztañaga (2011).

The median value of $\Delta\chi^2$ is slightly more negative when the fit is performed using the fiducial model versus when it is performed using *poly0* both before and after reconstruction. However, we see that even the simple *poly0* fits favour a model containing BAO over one without BAO. Before reconstruction, about 53% of the mocks lie above the 3σ line and after reconstruction, about 82% lie above this line. These numbers are very similar to those obtained in the fiducial model case.

We have also performed this experiment for a few other fitting ranges ($50\text{-}200h^{-1}$ Mpc and $70\text{-}150h^{-1}$ Mpc). The former yielded similar results, however, the latter had slightly less dramatic $\Delta\chi^2$ values. This is not unexpected because in these cases, the $A(r)$ terms are less constrained and can therefore absorb some of the BAO signal.

5 LASDAMAS REAL SPACE RESULTS

5.1 Covariance Matrices

As in redshift space, the covariance matrix derived from the mock correlation functions through Equation (3) is noisy. Hence, we again use a modified Gaussian covariance matrix as a smooth approximation to the mock covariance matrix.

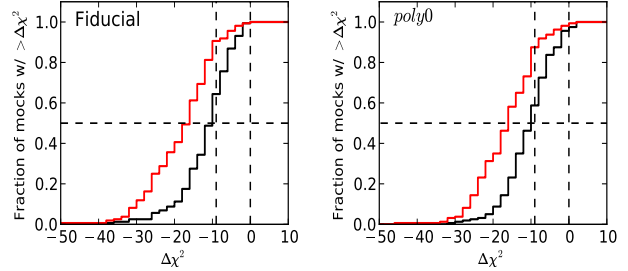


Figure 15. The detectability of the BAO feature in redshift space before and after reconstruction. (left) The normalized cumulative distribution function of $\Delta\chi^2 = \chi_{\text{BAO}}^2 - \chi_{\text{no BAO}}^2$ from fits using the fiducial $A(r)$ term. The solid black line shows the distribution before reconstruction and the solid red line shows the distribution after reconstruction. The horizontal dashed black line at fraction=50% indicates the value of $\Delta\chi^2$ that splits the mocks in half (i.e. the median $\Delta\chi^2$ value). We can see that the average $\Delta\chi^2$ is negative in both of these cases. The vertical dashed black lines indicate where $\Delta\chi^2 = 0$ and -9 (3σ). (right) The distribution of $\Delta\chi^2$ values from fits using *poly0*. Again the average $\Delta\chi^2$ is negative both before and after reconstruction. In all cases, the majority of mocks lie beyond the 3σ line, especially in the reconstructed case. This indicates that a detection of the BAO in our mock data is favoured over a non-detection.

However, in real space, we do not have any redshift-space observational effects such as Kaiser squashing or FoG. Therefore, we take the input power spectrum to the covariance matrix calculation to be

$$P_c(k) = b_0^2 P_t(k) \quad (33)$$

where the value of b_0^2 is determined as it was in redshift space.

We then introduce similar modification parameters to the redshift-space case, namely, we assume the covariance matrix can be modeled by the form

$$C_{ij}^m = 2 \int \frac{k^2 dk}{2\pi^2} \Delta_{j1}(kr_i) \Delta_{i1}(kr_j) \mathfrak{P}^2(k; c_0, c_2) + c_3. \quad (34)$$

Here, $\mathfrak{P}^2(k; c_0, c_2)$ corresponds to an $I^2(k)$, Equation (15), in which we make the substitution

$$P_c(k) + \frac{1}{\bar{n}(z)} \rightarrow c_0 P_c(k) + \frac{c_2}{\bar{n}(z)}. \quad (35)$$

Note that this is the same as Equation (19) except with $c_1 = 0$ and a different form for $P_c(k)$. Using the same maximum likelihood prescription as that described in §3.2, we can derive values for the modification parameters c_0 , c_2 and c_3 .

We use $\Sigma_{\text{nl}} = 7h^{-1}$ Mpc for calculating $P_c(k)$ in real space before reconstruction. As in the redshift-space case, the value of Σ_{nl} used has negligible effect on the derived matrix. With this $P_c(k)$ we find $c_1 = 0.98$, $c_2 = 1.50$ and $c_3 = 5.57 \times 10^{-8}$.

After reconstruction, we take $\Sigma_{\text{nl}} = 3h^{-1}$ Mpc in real space. The modified Gaussian covariance matrix we obtain has the modification parameters $c_0 = 0.89$, $c_2 = 1.57$ and $c_3 = 8.85 \times 10^{-8}$.

5.2 Fitting Forms

We use the same fiducial fitting form in both real space with and without reconstruction as in redshift space for measuring the shift in the acoustic scale, α . This is described by Equations (25 & 26). In real space before reconstruction, we define the fiducial model to make use of this fiducial form with $\xi_m(r)$ derived from the LasDamas cosmology and $\Sigma_{\text{nl}} = 7h^{-1}$ Mpc over a fitting range of $30 < r < 200h^{-1}$ Mpc. If we fit the average mock real-space correlation function allowing Σ_{nl} to vary, we obtain $\alpha = 1.002$ and $\Sigma_{\text{nl}} = 6.6h^{-1}$ Mpc, so our assumption for Σ_{nl} is not bad. In practice, like in redshift space, the measured α values for each individual mock are insensitive to our choice of Σ_{nl} as is shown in Table 3. The error bars on our mock data are approximated by the modified Gaussian covariance matrix (MGCM) derived in the previous section.

Fitting the average of the reconstructed real-space mock correlation functions while allowing Σ_{nl} to vary gives $\alpha = 0.999$ and $\Sigma_{\text{nl}} = 3.0h^{-1}$ Mpc. As in redshift space, the value of α prior to reconstruction is already very close to 1 and hence, we do not expect reconstruction to shift the acoustic peak much closer to its predicted linear theory position. However, Σ_{nl} decreased by a factor of ~ 2.2 from its pre-reconstruction value, implying that reconstruction was effective at removing the smearing of the acoustic peak caused by non-linear structure growth.

In our fiducial model for real space after reconstruction, we take $\Sigma_{\text{nl}} = 3h^{-1}$ Mpc, as we did in the calculation of the modified Gaussian covariance matrix. All other parameters of the fiducial model are analogous to the unreconstructed case described above. The same fitting algorithm as described in §3.3 is used.

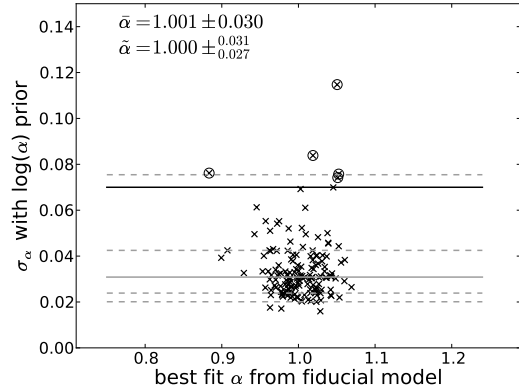


Figure 16. The standard deviations measured from $p(\alpha)$ versus the best-fit values of α from the fiducial model for each mock in real space. We impose a cutoff at a standard deviation of 7% (marked by the black horizontal line) as in redshift space. There are 5 mocks that lie above this line (circled in black). We take these mocks to have poorly measured values of α and discard them from our sample. The mean and median value of α after discarding these poorly constrained mocks are given on the plot.

5.3 Without Reconstruction Fitting Results

We use the same technique as that described in §4.1 to identify and remove the mock correlation functions that do not provide a well constrained measurement of α from our fitting sample. The corresponding real-space plot to Figure 7 is shown in Figure 16. We use the same 7% cutoff in standard deviation (σ_α) as in redshift space. This is marked by the black horizontal line. There are 5 mocks ($\sim 3\%$) that lie above this cut off (circled in black) which we take to have poorly constrained values of α and discard from our sample. The mean and median values of α after removing these poorly constrained mocks are indicated on the plot.

We test the robustness of our covariance matrix modeling and the fiducial model as we did in redshift space. Namely, we compare the values of α we measure using the fiducial model to those measured using a model in which the fiducial parameters are slightly changed, or by a fit in which we use the mock covariances rather than the MGCM. The resultant α , $\Delta\alpha$ and χ^2 values are given in Table 3. Note that in general, the values of $\Delta\alpha$ and their scatters are slightly smaller in real space than in redshift space. This is not unexpected since observational effects in redshift space such as FoG and Kaiser squashing tend to broaden the acoustic peak further, making it more difficult to obtain a precise measurement.

The results listed in Table 3 indicate that the trends in real space are the same as those found in redshift space. In particular, the values of α measured by slightly changing the input cosmology, Σ_{nl} , the order of $A(r)$ and the fitting range are consistent with the values measured using the fiducial model, usually with $\Delta\alpha < 0.2\%$. As in redshift space, the worst case is when we change the template to use $N_{\text{rel}} = 4$; this has a deviation of 0.6%. Again, this is likely the result of the $N_{\text{rel}} = 4$ correlation function template having a BAO peak that does not quite match the mocks well enough. If we go to less sensible Σ_{nl} such as $\Sigma_{\text{nl}} = 0h^{-1}$ Mpc, or decide to not use an $A(r)$ term, or fit using a less optimal fitting range,

Table 3. Real space fitting results for various models

Model	$\bar{\alpha}$	$\tilde{\alpha}$	$\overline{\Delta\alpha}^1$	$\widetilde{\Delta\alpha}$	$\overline{\chi^2/dof}$
Real Space without Reconstruction					
Fiducial [<i>f</i>]	1.001 ± 0.030	$1.000 \pm_{0.027}^{0.031}$	–	–	53.34/52
Fit with 15% larger Ω_m using fiducial $A(r)$. ²	1.000 ± 0.030	$0.999 \pm_{0.028}^{0.031}$	-0.001 ± 0.001	$-0.001 \pm_{0.001}^{0.001}$	53.58/52
Fit with $n_s = 0.96$ using fiducial $A(r)$.	1.002 ± 0.030	$1.001 \pm_{0.027}^{0.030}$	0.001 ± 0.001	$0.001 \pm_{0.000}^{0.001}$	53.39/52
Fit with $N_{rel} = 4$ using fiducial $A(r)$.	1.007 ± 0.030	$1.005 \pm_{0.027}^{0.030}$	0.006 ± 0.001	$0.005 \pm_{0.001}^{0.001}$	53.36/52
Fit with $\Sigma_{nl} \rightarrow 0$.	0.998 ± 0.032	$0.997 \pm_{0.029}^{0.032}$	-0.003 ± 0.013	$-0.003 \pm_{0.012}^{0.009}$	53.79/52
Fit with $\Sigma_{nl} \rightarrow \Sigma_{nl} + 2$.	1.003 ± 0.030	$1.003 \pm_{0.031}^{0.031}$	0.002 ± 0.005	$0.002 \pm_{0.005}^{0.004}$	53.83/52
Fit with <i>poly0</i> .	0.999 ± 0.031	$1.001 \pm_{0.031}^{0.030}$	-0.002 ± 0.008	$-0.001 \pm_{0.007}^{0.006}$	56.19/55
Fit with <i>poly2</i> .	1.000 ± 0.030	$0.999 \pm_{0.028}^{0.031}$	-0.001 ± 0.003	$-0.001 \pm_{0.002}^{0.002}$	54.65/53
Fit with <i>poly4</i> .	1.001 ± 0.029	$1.000 \pm_{0.027}^{0.031}$	0.000 ± 0.000	$0.000 \pm_{0.000}^{0.000}$	52.03/51
Fit with $50 < r < 200h^{-1}$ Mpc fitting range.	1.002 ± 0.029	$1.001 \pm_{0.025}^{0.031}$	0.001 ± 0.003	$0.001 \pm_{0.003}^{0.003}$	46.18/45
Fit with $20 < r < 200h^{-1}$ Mpc fitting range.	1.002 ± 0.028	$1.000 \pm_{0.026}^{0.029}$	0.001 ± 0.006	$0.002 \pm_{0.006}^{0.005}$	59.33/57
Fit with $70 < r < 150h^{-1}$ Mpc fitting range.	1.002 ± 0.031	$0.999 \pm_{0.020}^{0.031}$	0.001 ± 0.011	$0.001 \pm_{0.008}^{0.008}$	21.99/22
Fit using mock covariance matrix.	1.002 ± 0.023	$1.003 \pm_{0.025}^{0.021}$	0.001 ± 0.016	$0.002 \pm_{0.016}^{0.013}$	53.15/52
Real Space with Reconstruction					
Fiducial [<i>f</i>]	0.998 ± 0.020	$0.999 \pm_{0.019}^{0.019}$	–	–	53.44/52
Fit with 15% larger Ω_m using fiducial $A(r)$. ²	0.998 ± 0.020	$0.999 \pm_{0.020}^{0.019}$	-0.001 ± 0.002	$-0.000 \pm_{0.001}^{0.001}$	53.78/52
Fit with $n_s = 0.96$ using fiducial $A(r)$.	0.999 ± 0.020	$1.000 \pm_{0.019}^{0.020}$	0.001 ± 0.001	$0.001 \pm_{0.001}^{0.001}$	53.48/52
Fit with $N_{rel} = 4$ using fiducial $A(r)$.	1.003 ± 0.020	$1.003 \pm_{0.019}^{0.020}$	0.004 ± 0.001	$0.004 \pm_{0.000}^{0.001}$	53.68/52
Fit with $\Sigma_{nl} \rightarrow 0$.	0.998 ± 0.020	$0.999 \pm_{0.020}^{0.021}$	-0.000 ± 0.002	$-0.000 \pm_{0.002}^{0.002}$	53.47/52
Fit with $\Sigma_{nl} \rightarrow \Sigma_{nl} + 2$.	0.999 ± 0.020	$0.999 \pm_{0.019}^{0.020}$	0.000 ± 0.003	$0.001 \pm_{0.003}^{0.002}$	53.66/52
Fit with <i>poly0</i> .	0.997 ± 0.021	$0.999 \pm_{0.020}^{0.019}$	-0.001 ± 0.005	$-0.001 \pm_{0.004}^{0.003}$	56.44/55
Fit with <i>poly2</i> .	0.998 ± 0.020	$0.999 \pm_{0.021}^{0.019}$	-0.001 ± 0.002	$-0.001 \pm_{0.001}^{0.001}$	54.82/53
Fit with <i>poly4</i> .	0.998 ± 0.020	$0.999 \pm_{0.019}^{0.019}$	0.000 ± 0.000	$-0.000 \pm_{0.000}^{0.000}$	52.00/51
Fit with $50 < r < 200h^{-1}$ Mpc fitting range.	0.999 ± 0.020	$1.001 \pm_{0.020}^{0.019}$	0.001 ± 0.002	$0.001 \pm_{0.002}^{0.001}$	46.80/45
Fit with $20 < r < 200h^{-1}$ Mpc fitting range.	0.996 ± 0.020	$0.999 \pm_{0.021}^{0.018}$	-0.002 ± 0.004	$-0.001 \pm_{0.004}^{0.002}$	58.24/57
Fit with $70 < r < 150h^{-1}$ Mpc fitting range.	0.999 ± 0.021	$1.000 \pm_{0.022}^{0.019}$	0.001 ± 0.007	$0.001 \pm_{0.005}^{0.004}$	21.89/22
Fit using mock covariance matrix.	0.999 ± 0.017	$1.001 \pm_{0.019}^{0.014}$	0.001 ± 0.012	$-0.000 \pm_{0.010}^{0.010}$	52.85/52

¹ $\Delta\alpha = \alpha_{[i]} - \alpha_{[f]}$, where *i* is the model number.² We scale the measured sound horizons to the LasDamas cosmology where necessary.

the scatter in $\Delta\alpha$ increases as it did in redshift space. Noise in the mock covariance matrix is again the likely culprit causing the larger scatter in $\Delta\alpha$ between the MGCM fits and the mock covariance fits. These results all imply that our covariance modeling and our fiducial model are generally robust in real space as well.

5.4 With Reconstruction Fitting Results

As in redshift space, we find that after reconstruction, we are able to obtain much tighter constraints on the α values measured from each individual mock in real space. Figure 17 demonstrates this by plotting the standard deviation of $p(\alpha)$ for each mock before reconstruction against the value obtained after reconstruction. Note that this is the analogue to Figure 11 for redshift space. One can once again see that

most of the points lie significantly below the 1-1 line which indicates that reconstruction effectively sharpened up the acoustic peak allowing for more robust detections. The median decrease in standard deviation is 0.8% and there are no longer any mocks that lie above our σ_α cutoff of 7%.

Next, we once again test how slightly adjusting the fiducial model parameters affects our measurements of α . The results from these fits are given in Table 3. One can see that after reconstruction, the scatters in α are very similar between real space and redshift space.

We see that changing the fitting template cosmology, adjusting the value of Σ_{nl} , changing the order of $A(r)$ and altering the fitting range mostly have little effect on the value of α measured. The only case with $\Delta\alpha$ worse than 0.2% is the $N_{rel} = 4$ case, which measures 0.4%. In general, we still find that our fiducial model and our prescription for

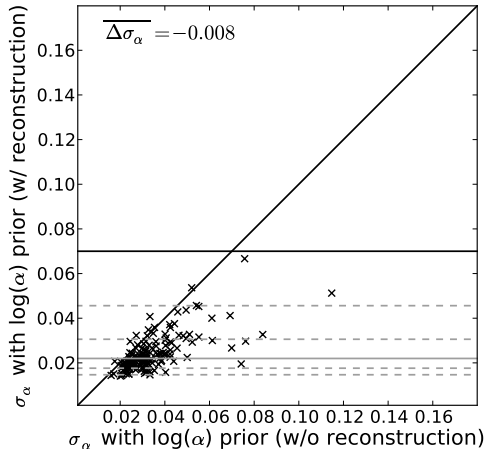


Figure 17. The analogous plot in reconstructed real space to Figure 11 for reconstructed redshift space. Once again, most of the points lie significantly below the 1-1 line. The median decrease in standard deviation is $\sim 0.8\%$ as shown in the plot. Note that there are no longer any poorly constrained mocks with standard deviations above our 7% cutoff. This once again illustrates how useful and effective reconstruction is.

deriving a suitable covariance matrix such as the MGCM are robust. These results are all consistent with previous results.

Lastly, we investigate the detectability of the BAO in both unreconstructed and reconstructed real space. We find that the median $\Delta\chi^2 = \chi_{\text{BAO}}^2 - \chi_{\text{no BAO}}^2$ values are again negative and similar in magnitude to the redshift-space cases. This suggests that the data is better fit by a model containing BAO rather than a model without BAO. We also note that the post-reconstruction real-space $\Delta\chi^2$ values are more negative than before reconstruction. Hence, we conclude that we have a firm detection of the acoustic signal in our mocks, with the detection being even more robust after reconstruction.

6 MEASURING THE BAO IN SDSS DR7

6.1 Covariance Matrices

In this section, we apply the techniques described in §3 for redshift space to the DR7 LRG full sample. We use the form for the modified Gaussian covariance matrix given in Equation (18) for redshift space with and without reconstruction. We adopt the modification parameters (c_0 , c_1 , c_2 and c_3) derived for the LasDamas mocks in both of these cases, assuming that the overall shape of the covariance matrix should be modified in the same way for both DR7 and LasDamas. However, we now switch to the WMAP7 cosmology in constructing $P_c(k)$.

The b_0^2 coefficient in Equation (12) is chosen such that $P_c(k)$ matches the DR7 correlation function at $r = 50h^{-1}$ Mpc. This again ensures that the amplitude of $P_c(k)$ matches the clustering amplitude of DR7, an essential condition when reusing the modification parameters to adjust the shape of the Gaussian covariance matrix.

In computing the pre-reconstruction covariance matrix, we retain $\Sigma_{\text{nl}} = 8h^{-1}$ Mpc and for post-reconstruction, we retain $\Sigma_{\text{nl}} = 4h^{-1}$ Mpc. We also note that since the DR7

Table 4. DR7 fit results for various models

Model	α	χ^2
Redshift Space without Reconstruction		
Fiducial [f]	1.017 ± 0.035^1	47.71/52
$\Sigma_{\text{nl}} = 0$	1.025 ± 0.029	49.89/52
$\Sigma_{\text{nl}} \rightarrow \Sigma_{\text{nl}} + 2$	1.011 ± 0.039	47.86/52
<i>poly0</i>	1.002 ± 0.038	55.35/55
<i>poly2</i>	1.016 ± 0.034	47.72/53
<i>poly4</i>	1.016 ± 0.039	42.74/51
50 – 200 h^{-1} Mpc fitting range	1.011 ± 0.040	40.44/45
Redshift Space with Reconstruction		
Fiducial [f]	1.012 ± 0.019	36.82/52
$\Sigma_{\text{nl}} = 0$	1.012 ± 0.017	35.99/52
$\Sigma_{\text{nl}} \rightarrow \Sigma_{\text{nl}} + 2$	1.012 ± 0.021	38.12/52
<i>poly0</i>	1.007 ± 0.020	47.18/55
<i>poly2</i>	1.012 ± 0.019	37.14/53
<i>poly4</i>	1.012 ± 0.019	36.34/51
50 – 200 h^{-1} Mpc fitting range	1.012 ± 0.019	33.21/45

¹ Here, the quoted α is the best-fit value rather than the mean of the probability distribution $p(\alpha)$ as in Paper I. These 2 values may be slightly different but are well within error of each other.

data goes out to $z = 0.47$, we extend our $\bar{n}(z)$ model derived from the LasDamas random catalogue out to $z = 0.47$ as well, after scaling it to the WMAP7 cosmology.

6.2 Fit Results

We compute the DR7 correlation functions in the WMAP7 cosmology. For details of the computation and reconstruction, please see Paper I. We present only the fitting results here.

Figure 18 shows the results of our fits to the DR7 data using the fiducial model and fitting algorithm outlined in §3. These results are also summarized in Table 4 along with the fit results from varying fiducial model parameters such as Σ_{nl} and fitting range.

The 2 panels at the top illustrate the pre-reconstruction results and the 2 panels at the bottom illustrate the post-reconstruction results. We fix Σ_{nl} in our model templates to the same values as in the covariance matrices. The left column shows the data with the fiducial model fit overplotted (black line). The dashed red line corresponds to a fit using *poly0* instead of fiducial $A(r)$. The best-fit α and χ^2 values are quoted on the plot. The right column shows the $p(\alpha)$ distributions for the fits using the fiducial model (black line) and the fits using *poly0* (red line). The means of the distributions are quoted on the plot along with their standard deviations σ_α . Taking the best-fit α value from the fiducial model fit and the σ_α from the $p(\alpha)$ distribution, we measure the DR7 acoustic scale to correspond to $\alpha = 1.017 \pm 0.035$ before reconstruction and $\alpha = 1.012 \pm 0.019$ after reconstruction. Using the mean of the $p(\alpha)$ probability distribu-

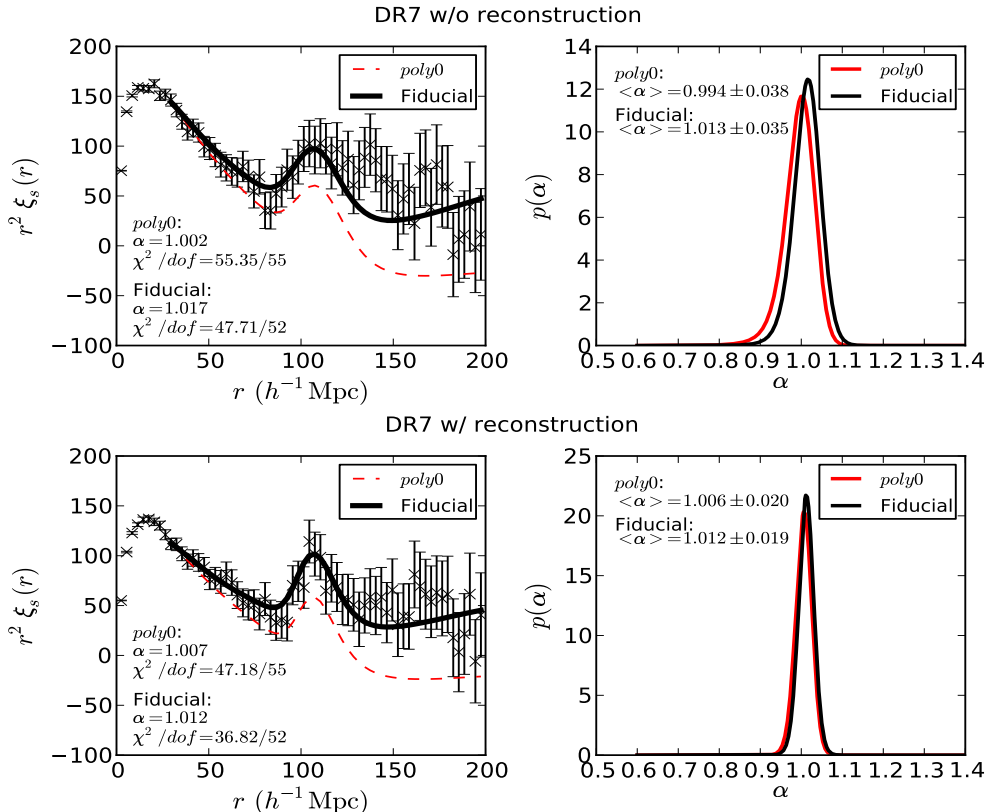


Figure 18. DR7 fit results. (top) Before reconstruction. (bottom) After reconstruction. The left column shows the fits to the DR7 data using the fiducial model (solid black line) and *poly0* (dashed red line). The right column shows the $p(\alpha)$ distributions for fits using the fiducial model (black line) and *poly0* (red line). Here we have again applied the 15% prior in $\log(\alpha)$ as described in §4.1. As with the LasDamas mocks, we use $\Sigma_{\text{nl}} = 8h^{-1}$ Mpc in the fiducial model before reconstruction and $\Sigma_{\text{nl}} = 4h^{-1}$ Mpc after reconstruction. The similarities in χ^2 , α and σ_α between the fiducial and *poly0* cases indicate that the covariance matrix does not demand an $A(r)$ term in the model. However, our mock correlation function analyses suggest that having an $A(r)$ term is useful for marginalizing out errors due to assuming the wrong cosmology and broadband effects that are not included in our fitting model. The effectiveness of $A(r)$ in marginalizing over the conspicuous excess large-scale power seen in these DR7 correlation functions (left panels) also exemplifies its utility.

tion instead gives $\alpha = 1.013 \pm 0.035$ before reconstruction and $\alpha = 1.012 \pm 0.019$ after reconstruction. One can see that the two values are the same after reconstruction, however, they are slightly different before reconstruction due to the slight asymmetry of the $p(\alpha)$ distribution. The pre-reconstruction error is comparable to the 3.3% found by Percival et al. (2010) for a similar sample.

This factor of 1.8 decrease in the error after applying reconstruction is similar to what we saw for the mock catalogues. Since the survey volume required to achieve a certain variance is inversely proportional to the variance, we would have to increase the survey volume by about a factor of 3 to achieve this same reduction in the error. This clearly shows how effective reconstruction is at improving our measurement of the acoustic scale. We can convert these α values into $D_v(z)/r_s$ measurements at a median redshift of $z = 0.35$ according to Eisenstein et al. (2005), i.e.

$$\alpha = \frac{D_v(z)/r_s}{D_{v,f}(z)/r_{s,f}} \quad (36)$$

where the subscript f denotes the fiducial WMAP7 cosmology, $D_v(z)$ is the spherically averaged distance to redshift z and r_s is the sound horizon. In the WMAP7 cosmology

we have $r_{s,f} = 152.76$ Mpc and $D_{v,f}(z) = 1340.2$ Mpc. The best-fit α values then give $D_v(z)/r_s = 8.92 \pm 0.31$ before reconstruction and $D_v(z)/r_s = 8.88 \pm 0.17$ after reconstruction. The means of the $p(\alpha)$ distributions give $D_v(z)/r_s = 8.89 \pm 0.31$ before reconstruction and $D_v(z)/r_s = 8.88 \pm 0.17$ after reconstruction.

From Table 4, we see that the α values obtained by varying Σ_{nl} , order of $A(r)$ and fitting range are all consistent with each other within the errors. In particular, after reconstruction, we see that all cases have very similar errors and all give an α value within 0.1% of the others except the *poly0* case. This is as expected from our analysis of the mock catalogues.

The DR7 correlation function exceeds the linear theory prediction at large r , suggesting extra large-scale power. This can be seen in Figure 18 by comparing the data to the fit using the $A(r) = 0$ model (dashed red line). While this offset appears large to the eye, we stress that the data points are correlated such that these coherent offsets are only weakly constrained. This is demonstrated by the fact that the fiducial $A(r)$ fit, which adds three marginalization parameters and largely compensates the offset, does not de-

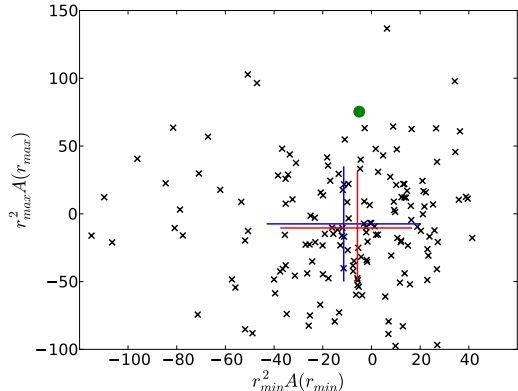


Figure 19. The values of the fiducial $A(r)$ term at the edges of the fitting range for the 160 LasDamas mocks (black crosses) in redshift space before reconstruction. The large blue cross indicates the mean and standard deviation. The large red cross indicates the median and 16th/84th percentile levels. The DR7 point is overplotted as the green circle. One can see that this point falls within 2σ of the LasDamas average which implies that the shape of the DR7 $A(r)$ term is not unexpected. Hence, even though $A(r)$ is providing a significant amount of marginalization to account for the excess power at large scales in the DR7 correlation function, it is not an inordinately large amount in the context of LasDamas.

crease χ^2 by a very significant amount. Hence, while such extra power could be a sign of unaddressed systematic errors in the data set or some exotic cosmology, the statistical significance of the extra power is weak. In addition, the measured α and σ_α values are consistent, which suggests that the data does not strongly demand a non-zero $A(r)$ in the model. However, we see that the fiducial $A(r)$ fit matches the data much better. Also, our analysis of the mock correlation functions indicates that we should err on the side of caution and marginalize over a non-zero $A(r)$ term to remove any broadband affects not accounted for in the model that could bias our measurement of the acoustic scale.

To further address the excess large-scale power, we study whether the magnitude of the fiducial $A(r)$ term in the best-fit model to the DR7 data is unusual in the context of the LasDamas mocks. Figure 19 shows the values of the $A(r)$ term at the edges of the fitting range (i.e. at $r \sim 30h^{-1}$ Mpc and $r \sim 200h^{-1}$ Mpc) for the LasDamas mocks before reconstruction (black crosses). The large blue cross indicates the mean and standard deviation of the LasDamas values and the large red cross indicates the median and the 16th/84th percentiles. The DR7 point is overplotted as the green circle and clearly falls within 2σ of the LasDamas average. A similar plot can be made for the post-reconstruction fits.

6.3 Comparison with LasDamas Cosmology

We also compute the DR7 correlation functions with and without reconstruction using the LasDamas cosmology. We apply the same fitting algorithm, but change the cosmology of the covariance matrix and template model to that of LasDamas. We again adopt the LasDamas modification parameters to the Gaussian covariance matrix and the same Σ_{nl} values.

We find $\alpha = 1.053 \pm 0.034$ in redshift space before reconstruction and $\alpha = 1.044 \pm 0.019$ after reconstruction. Converting these α values to D_v/r_s at a median redshift of $z = 0.35$, we find $D_v/r_s = 8.95 \pm 0.30$ before reconstruction and $D_v/r_s = 8.87 \pm 0.17$ after reconstruction. These values are consistent with those obtained from the DR7 data in the WMAP7 cosmology when we factor in errors. The values of σ_α are also consistent.

6.4 Significance of the BAO Detection

The BAO detection significance is an obvious question that must be addressed. However, its characterization is non-trivial. There are essentially 2 different tests which need to be evaluated. The first considers the possibility that we have not detected the BAO signal in our data, either because it does not actually exist or we just have not observed it. The second assumes the BAO peak does exist and asks how robustly we have measured its location.

We attempt to address these 2 questions in Figure 20. In the top panels we have plotted $\Delta\chi^2 = \chi_{\text{BAO}}^2 - \chi_{\text{no BAO}}^2$ at various values of α for different $A(r)$. As in Figure 15, the χ_{BAO}^2 values are obtained through fits using a model containing BAO and the $\chi_{\text{no BAO}}^2$ are obtained through fits using a model without BAO. The left panel shows the results before reconstruction and the right panel shows the results after reconstruction. These plots answer the first question of whether we have detected the BAO assuming that we are fairly confident in our cosmology. With this assumption, we know that α must be close to 1 and hence we can restrict our attention to this region. One can see that the $\Delta\chi^2$ values are all negative around $\alpha = 1$ and reach a minimum of $\Delta\chi^2 \sim -11$ before reconstruction and ~ -18 after reconstruction for the fiducial $A(r)$ fits (solid black line). This indicates that a model containing BAO is favoured over a model without BAO at more than 3σ ($\Delta\chi^2 = -9$) confidence before reconstruction and more than 4σ ($\Delta\chi^2 = -16$) confidence after reconstruction. Note that these $\Delta\chi^2$ values are comparable to the median values we measured for the LasDamas mocks (-10 and -16 respectively). While it is true that these χ^2 values are not directly comparable due to the volume difference between DR7 in a LasDamas cosmology and a WMAP7 cosmology, this discrepancy is small. Hence, DR7 should be a fairly typical sample consistent with cosmic variance.

The bottom panels show $\Delta\chi^2 = \chi^2(\alpha) - \chi_{\text{min}}^2$ versus α for various $A(r)$. Here, χ_{min}^2 is the value of χ^2 that corresponds to the best-fit value of α . These plots are similar to the middle columns of Figures 6 and 10. They answer the second question of whether the BAO scale we measure is significantly favoured over other values. Again, the left column corresponds to the results before reconstruction and the right column corresponds to the results after reconstruction. For the fiducial $A(r)$ fit before reconstruction, the curve is parabolic around the best-fit α indicating the Gaussian nature of α . The corresponding χ_{min}^2 lies at $\Delta\chi^2 \sim 10 - 15$ below where the curve starts plateauing. Recall that the plateau is due to the fitter having an easier time hiding the acoustic peak in the errors at large r and is not actually physical. Post-reconstruction, the parabola becomes tighter around the best-fit α and the χ^2 difference between the minimum and the plateau grows to 25. This indicates that while

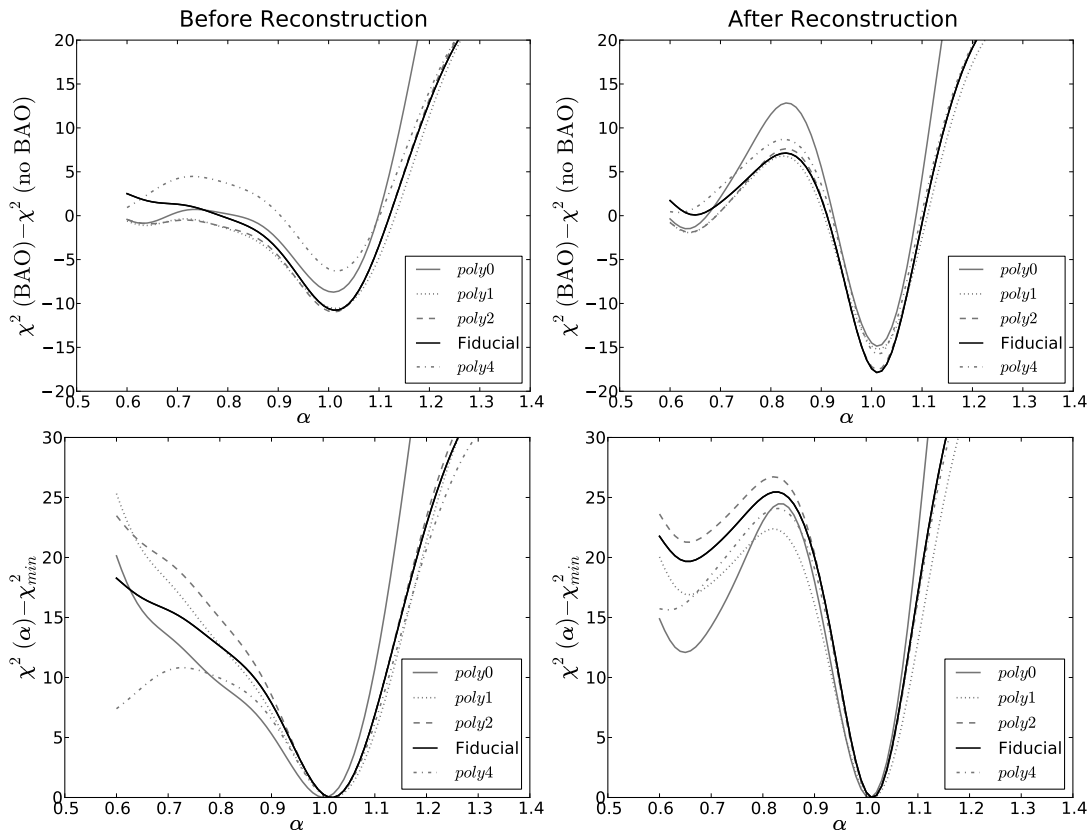


Figure 20. Significance of the BAO in the DR7 data. (top) $\Delta\chi^2 = \chi^2_{\text{BAO}} - \chi^2_{\text{no BAO}}$ versus α for different $A(r)$ before reconstruction (left) and after reconstruction (right). The different forms of $A(r)$ are represented by different line styles as indicated in the legend. For our fiducial form (solid black line), $\Delta\chi^2$ reaches a minimum of ~ -11 before reconstruction and ~ -18 after reconstruction. Hence, a model containing BAO is a better fit to the data than a model without BAO at more than 3σ significance ($\Delta\chi^2 = -9$) before reconstruction and at more than 4σ significance ($\Delta\chi^2 = -16$) after reconstruction. (bottom) $\Delta\chi^2 = \chi^2(\alpha) - \chi^2_{\min}$ versus α for different $A(r)$ before reconstruction (left) and after reconstruction (right). For our fiducial form, the curve is parabolic around the minimum that corresponds to the best-fit value of α . Before reconstruction, the χ^2 difference between the minimum and where the curve starts plateauing at small α is $\sim 10 - 15$. This difference becomes even more pronounced after reconstruction, measuring a $\Delta\chi^2 \sim 25$. Hence, the measured acoustic scale is favoured at slightly more than 3σ ($\Delta\chi^2 = 9$) before reconstruction and at 5σ ($\Delta\chi^2 = 25$) post-reconstruction. Both the top and bottom panels show an increase in significance of the BAO detection after reconstruction. Also, one can see that in general (and especially before reconstruction), the fits with higher order $A(r)$ terms (i.e. *poly2* and fiducial) have more prominent $\Delta\chi^2$ minima in both the top and bottom panels. This indicates that we obtain more robust BAO detections when fitting with non-trivial $A(r)$ terms. However, fits with *poly4* appear to perform worse than the lower order fits before reconstruction. This indicates that we are likely beginning to afford the model too much flexibility.

the measured acoustic scale is favoured at slightly more than 3σ ($\Delta\chi^2 = 9$) before reconstruction, after reconstruction, it becomes favoured at 5σ ($\Delta\chi^2 = 25$). Hence, reconstruction increases the BAO detection significance in both of the tests considered here.

Another point to note is that in general, the $\Delta\chi^2$ minima in both of the above mentioned cases is more prominent when one fits with a higher degree $A(r)$ (i.e. *poly2* or fiducial). This is especially true before reconstruction when the acoustic scale is more difficult to measure due to non-linear effects. Hence, we see that a more robust BAO detection is achieved when fitting with a non-zero $A(r)$. However, we also see that before reconstruction, *poly4* (dash-dotted line) performs worse than the lower order fits. This is because when we give the model too much freedom, it acquires more flexibility to hide the acoustic peak in the errors at large r

while using the $A(r)$ nuisance terms to compensate for the shape of the acoustic peak in the data.

7 CONCLUSIONS

We develop a series of tools and methods to study the baryon acoustic oscillations in the SDSS DR7 LRG sample. These allow us to carefully treat the uncertainties and covariances involved in measuring the acoustic scale. Such tools include reconstruction, an algorithm for estimating a reliable covariance matrix and a robust fitting model for the correlation function. In this study, we demonstrate the first application of reconstruction to a galaxy redshift survey and more careful treatments of the covariance matrix and fitting model. This paper is the second in a series of three papers. Paper I discusses the details of the DR7 LRG sample and our re-

construction technique. Paper III discusses the cosmological implications of our measured acoustic scale.

Through our analysis of 160 SDSS DR7 mock catalogues from the LasDamas simulations, we find that the covariance matrix derived directly from the mocks is very noisy. We present a new method for obtaining a smooth approximation to the mock covariance matrix using the analytic Gaussian covariance matrix. This process introduces appropriate modifications to the Gaussian covariance matrix using a maximum likelihood fit to the mock covariances. We show that the modified Gaussian covariance matrix obtained this way is a good fit to the mock covariances and produces consistent measurements of the acoustic scale.

Some of the mocks have weak acoustic signals and hence the acoustic scale can be poorly determined in these. In order to identify these poorly constrained mocks, we find that looking at the probability distribution of the shift in the acoustic scale, α , can be a good gauge. For mocks that have distributions with a larger standard deviation, the constraint on α is poorer and vice versa. We impose a cutoff at a standard deviation of 7% in our mocks and find that in redshift space, 8 mocks lie above this cutoff and in real space, 5 do. After reconstruction, no poorly constrained mocks remain in redshift or real space.

We find that in redshift space, we obtain consistent measurements of α when the fiducial model parameters (template cosmology, Σ_{nl} , degree of $A(r)$ and fitting range) are slightly tweaked. This implies that the values of α we measure are robust against small changes in model parameters. Hence, our fiducial model should return reliable measurements of the acoustic scale. However, we note that in order to afford the model enough flexibility, $A(r)$ should be non-zero as in the fiducial form, Equation (26). This is because the $A(r)$ term is required to marginalize out all the broadband contributions not accounted for by the template such as scale-dependent bias and redshift-space distortions (or residual redshift-space distortions in the post-reconstruction case). This term also accounts for any errors in our choice of model cosmology. We find that if we use a template cosmology that does not match the simulations to perform the fit, a low order $A(r)$ does not recover the correct acoustic scale as well. One must also be careful not to use an $A(r)$ term that is very high order as the model will begin fitting the noise in the data.

Using our fitting scheme on our mock correlation functions, we consistently measure the acoustic scale to $\sim 3.3\%$ accuracy in redshift space before reconstruction and $\sim 2.1\%$ after reconstruction. The fit to the average redshift-space mock correlation function before reconstruction gives an α that is already very close to 1. Hence, we do not expect reconstruction to shift the acoustic scale much closer to its predicted linear theory position. However, the decrease in best-fit Σ_{nl} from $8.1h^{-1}$ Mpc before reconstruction to $4.4h^{-1}$ Mpc after reconstruction shows that reconstruction is effective at removing the smearing of the acoustic peak caused by non-linear structure growth.

We demonstrated the detectability of the acoustic signature in redshift space both before and after reconstruction. In both cases we fit each of the mocks using a model containing BAO and a model without BAO and find that $\Delta\chi^2 = \chi_{BAO}^2 - \chi_{no\ BAO}^2$ is negative on average. This indicates that the mock data prefers a model containing BAO

over a model without BAO. Hence, we conclude that we have a robust detection of the acoustic signal in our mocks. We note that $\Delta\chi^2$ is even more negative after reconstruction, again revealing the importance of the procedure. In addition, when we fit using *poly0*, we still obtain negative average values of $\Delta\chi^2$ implying that even with this simple model we can robustly detect the BAO in our mocks. Similar results are obtained in real space before and after reconstruction.

We then apply our covariance matrix and fitting techniques to the correlation function calculated from the DR7 data in the WMAP7 cosmology. We again vary the various parameters of the fit and recover consistent values of α . From the probability distribution of α we measure a mean $\alpha = 1.013 \pm 0.035$ before reconstruction which gives $D_v(z = 0.35)/r_s = 8.89 \pm 0.31$. After reconstruction we measure $\alpha = 1.012 \pm 0.019$ which gives $D_v(z = 0.35)/r_s = 8.88 \pm 0.17$. We see that the error on α has decreased by a factor of 1.8. Such a decrease is equivalent to what we would expect if we increase the survey volume by a factor of 3. This again demonstrates the power of reconstruction in removing the uncertainties introduced by non-linear structure growth.

Finally we assess the significance of our DR7 BAO measurement using 2 different tests. The first measures how confident we are that our data contains a BAO signature and the second measures how confident we are that our measurement of the BAO scale is correct. We find that before reconstruction, our data favours a model containing BAO at more than 3σ over a model without BAO and the acoustic scale we measure is preferred at more than 3σ . After reconstruction, these confidence levels become even more pronounced. The data favours a model containing BAO at more than 4σ and the measured acoustic scale is preferred at 5σ . Hence, we conclude that our DR7 BAO measurement is robust.

The methods developed in this paper and its companions should be applicable to future data sets with higher precision requirements such as the Baryon Oscillation Spectroscopic Survey (BOSS) in SDSS-III. BOSS aims to measure the acoustic scale to $\sim 1\%$ precision at $z = 0.35$ and $z = 0.6$ which will grant us even more precise measurements of the properties of dark energy.

8 ACKNOWLEDGMENTS

Funding for the Sloan Digital Sky Survey (SDSS) and SDSS-II has been provided by the Alfred P. Sloan Foundation, the Participating Institutions, the National Science Foundation, the U.S. Department of Energy, the National Aeronautics and Space Administration, the Japanese Monbukagakusho, the Max Planck Society and the Higher Education Funding Council for England. The SDSS website is <http://www.sdss.org/>.

The SDSS is managed by the Astrophysical Research Consortium (ARC) for the Participating Institutions. The Participating Institutions are the American Museum of Natural History, Astrophysical Institute Potsdam, University of Basel, University of Chicago, Drexel University, Fermilab, the Institute for Advanced Study, the Japan Participation Group, the Johns Hopkins University, the Joint Institute for Nuclear Astrophysics, the Kavli Institute for Particle Astrophysics and Cosmology, the Korean Scientist Group,

the Chinese Academy of Sciences (LAMOST), Los Alamos National Laboratory, the Max-Planck-Institute for Astronomy (MPIA), New Mexico State University, Ohio State University, University of Pittsburgh, University of Portsmouth, Princeton University, the United States Naval Observatory and the University of Washington.

We thank the LasDamas collaboration for making their galaxy mock catalogs public. We thank Cameron McBride for assistance in using the LasDamas mocks and comments on earlier versions of this work. We thank Martin White for useful conversations on reconstruction. XX thanks Hee-Jong Seo for her insightful comments. XX, DJE, and KTM were supported by NSF grant AST-0707725 and NASA grant NNX07AH11G. NP and AJC are partially supported by NASA grant NNX11AF43G. This work was supported in part by the facilities and staff of the Yale University Faculty of Arts and Sciences High Performance Computing Center.

REFERENCES

- Abdalla, F. B., & Rawlings, S., 2005, *MNRAS*, 360, 27
 Amendola, L., Quercellini, C., Giallongo, E., 2005, *MNRAS*, 357, 429
 Angulo, R., et al., 2005, *MNRAS*, 362, L25
 Angulo, R., et al., 2008, *MNRAS*, 383, 755
 Beutler, F., et al., 2011, *MNRAS*, 416, 3017
 Blake, C., & Glazebrook, K., 2003, *ApJ*, 594, 665
 Blake, C., et al., 2011, *MNRAS*, 415, 2892
 Blake, C., et al., 2011, *MNRAS*, 418, 1707
 Bond, J. R., & Efstathiou, G., 1984, *ApJ*, 594, 665
 Cabré, A., & Gaztañaga, E., 2011, *MNRAS*, 412, L98
 Cole, S., et al., 2005, *MNRAS*, 362, 505
 Crocce, M., & Scoccimarro, R., 2006, *Phys. Rev. D*, 73, 063520
 Crocce, M., & Scoccimarro, R., 2008, *Phys. Rev. D*, 77, 023533
 Dolney, D., Jain, B., & Takada, M., 2006, *MNRAS*, 366, 884
 Eisenstein, D. J., & Hu, W., 1998, *ApJ*, 496, 605
 Eisenstein, D. J., Hu, W., Tegmark, M., 1998, *ApJL*, 504, L57
 Eisenstein, D. J., 2003, in *ASP Conference Series*, volume 280, *Next Generation Wide Field Multi-Object Spectroscopy*, ed. M.J.I. Brown & A. Dey (ASP: San Francisco) pp. 35-43; astro-ph/0301623
 Eisenstein, D. J., et al., 2005, *ApJ*, 633, 560
 Eisenstein, D. J., Seo, H.-J., & White, M., 2007, *ApJ*, 664, 660
 Eisenstein, D. J., Seo, H.-J., Sirko, E., & Spergel, D. N., 2007, *ApJ*, 664, 675
 Glazebrook, K., & Blake, C., 2005, *ApJ*, 631, 1
 Guzik, J., Bernstein, G., & Smith, R. E., 2007, *MNRAS*, 375, 1329
 Hamilton, A. J. S., Rimes, C. D., & Scoccimarro, R., 2006, *MNRAS*, 371, 1188
 Ho, S., et al., 2012, *ApJ* submitted (arXiv:1201.2137)
 Holtzman, J. A., 1989, *ApJS*, 71, 1
 Hu, W., & Haiman, Z., 2003, *Phys. Rev. D*, 68, 063004
 Hu, W., & Sugiyama, N., 1996, *ApJ*, 471, 542
 Hu, W., & White, M., 1996, *ApJ*, 471, 30
 Zhan, H., Knox, L., & Tyson, J. A., 2009, *ApJ*, 690, 923
 Huff, E., et al., 2007, *Astroparticle Physics*, 26, 351
 Hütsi, G., 2006, *A&A*, 449, 891
 Jeong, D., & Komatsu, E., 2006, *ApJ*, 651, 619
 Kaiser, N., 1987, *MNRAS*, 227, 1
 Kazin, E., et al., 2010, *ApJ*, 710, 1444
 Komatsu, E., et al., 2010, *ApJS*, 192, 18
 Linder, E. V., 2003, *Phys. Rev. D*, 68, 083504
 Ma, Z., 2007, *ApJ*, 665, 887
 Mao, X.-C., & Wu, X.-P., 2008, *ApJ*, 673, L107
 Matsubara, T., 2004, *ApJ*, 615, 573
 Matsubara, T., 2007, *Phys. Rev. D*, 77, 063530
 Mehta, K., et al., 2011, *ApJ*, 734, 94
 Mehta, K., et al., in prep (Paper III)
 Meiksin, A., & White, M. Peacock, J. A., 1999, *MNRAS*, 304, 851
 McBride, C., et al., 2012, in prep
 Noh, Y., White, M., & Padmanabhan, N., 2009, *Phys. Rev. D*, 80, 123501
 Padmanabhan, N., et al., 2007, *MNRAS*, 378, 852
 Padmanabhan, N., & White, M., 2009, *Phys. Rev. D*, 80, 063508
 Padmanabhan, N., White, M., & Cohn, J. D., 2009, *Phys. Rev. D*, 79, 063523
 Padmanabhan, N., et al., in prep (Paper I)
 Percival, W. J., et al., 2007, *ApJ*, 657, 51
 Percival, W. J., et al., 2007, *MNRAS*, 381, 1053
 Percival, W. J., et al., 2010, *MNRAS*, 401, 2148
 Peebles, P. J. E., & Yu, J. T., 1970, *ApJ*, 162, 815
 Sanchez, A. G., Baugh, C. M., Angulo, R., 2008, 390, 1470
 Sanchez, A. G., et al., 2009, *MNRAS*, 400, 1643
 Scoccimarro, R., & Sheth, R. K., 2002, *MNRAS*, 329, 629
 Seo, H.-J., & Eisenstein, D. J., 2003, *ApJ*, 598, 720
 Seo, H.-J., & Eisenstein, D. J., 2005, *ApJ*, 633, 575
 Seo, H.-J., & Eisenstein, D. J., 2007, *ApJ*, 665, 14
 Seo, H.-J., Siegel, E. R., Eisenstein, D. J., White, M., 2008, *ApJ*, 686, 13
 Seo, H.-J., et al., 2010, *ApJ*, 720, 1650
 Seo, H.-J., et al., 2012, *ApJ* submitted (arXiv:1201.2172v1)
 Smith, R. E., Scoccimarro, R., Sheth, R. K., 2008, *Phys. Rev. D*, 77, 043525
 Sunyaev, R. A., & Zeldovich, Y. B., 1970, *Ap&SS*, 7, 3
 Tegmark, M., et al., 2006, *Phys. Rev. D*, 74, 123507
 Takahashi, R., et al., 2009, *ApJ*, 696, 93
 Wang, X., et al., 2009, *MNRAS*, 394, 1775
 Wyithe, J. S. B., Loeb, A., & Geil, P. M., 2008, *MNRAS*, 383, 1195
 Xu, X., et al., 2010, *ApJ*, 718, 1224